

Low-Rank Hankel Matrix Completion for Robust Time-Frequency Analysis

Shuimei Zhang, *Student Member, IEEE*, and Yimin D. Zhang, *Fellow, IEEE*

Abstract—In this paper, we develop a novel method to enable robust sparsity-based time-frequency representation of multi-component frequency modulated signals in the presence of burst missing samples, where the amplitudes of the different signal components are generally different. Unlike existing methods which require cross-term presence to be sparse in the time-frequency domain, the proposed method permits effective time-frequency representation reconstruction even when undesired cross-terms take a high occupancy. A key enabling procedure is the high-fidelity missing entry recovery of the instantaneous autocorrelation function that is insensitive to cross-terms. By designing instantaneous autocorrelation function patches such that their Doppler-frequency domain representation is sparse, we formulate the instantaneous autocorrelation function recovery problem as a patch-based low-rank block Hankel matrix completion problem. This approach effectively suppresses the effects of burst missing data samples and is robust to the amplitude differences. A data-adaptive time-frequency kernel is then applied to further mitigate the undesired cross-terms and the residual artifacts due to the burst missing samples. We prove the superiority of the proposed method over the state of the art for both multi-component linear and nonlinear frequency modulated signals. Simulation results confirm that the proposed method outperforms the state of the art for different types of frequency modulated signals with varying signal-to-noise ratios and missing sample rates.

Index Terms—Time-frequency analysis, burst missing samples, low-rank structured matrix completion, nonstationary signal, annihilating filter.

I. INTRODUCTION

NONSTATIONARY signals are widely observed in many real-world applications, such as radar, sonar, radio astronomy, communications, acoustics, and vibration systems [1]–[5]. One important class of nonstationary signals is frequency modulated (FM) signals, which are characterized by time-varying instantaneous frequencies (IFs) [6]–[10]. Compared to signals represented in either the time or frequency domain, joint time-frequency (TF) domain representation provides a time-varying spectrum to enable effective signal analysis, discrimination, and classification [9], [11].

In practice, missing data samples frequently occur during signal reception due to various reasons, e.g., propagation fading, measurement obstruction, removal of impulsive noise or narrowband interference, and intentional undersampling. For example, there are strong interests in radar applications to reduce the sampling rate in order to simplify the system complexity [12]–[14], and radar and radio astronomical data

are often processed after removing strong clutter and interference signals [15]–[17]. Electroencephalogram (EEG) data signals are often processed after removal of unrelated artifacts due to, e.g., eye movement and blink [18], [19]. Conventional methods are difficult to achieve reliable TF analysis and IF estimation in the presence of such missing or removed data.

Missing data samples in the time domain lend themselves to be missing entries in the instantaneous autocorrelation function (IAF) and induce artifacts in the TF representation (TFR). Recently, robust TFRs have been developed to handle the existence of random missing samples [20]–[23]. In these methods, it is revealed that TF kernels, in addition to their traditional functions of suppressing TF cross-terms, also effectively mitigate artifacts induced by the random missing samples. By taking advantages of the signal sparsity in the TF domain, these works also show that the effects of random missing samples can be further reduced by employing sparsity-based TFR reconstruction methods. In particular, an IAF slice vector (either a column or a row) can be represented as the summation of finite sinusoidal components. As such, the Fourier transform of an IAF slice along the time or the lag direction exhibits sparsity in the TF or ambiguity function (AF) domain. This fact enables effective sparsity-based TF analysis that mitigates the effects of missing samples. Note that it has been shown in [24], [25] that completing missing entries in the IAF domain is more effective than the counterpart carried out in the time domain.

In practice, missing samples are likely to appear as clusters when, e.g., the propagation fading and measurement obstruction periods exceed the sampling interval. Unlike the effects of random missing samples, which cause the artifacts to be uniformly spread over the entire TF domain, the artifacts due to burst missing samples are highly localized around the true IFs, rendering extremely challenging TF analyses for which the existing methods become ineffective [25]–[27].

To enable effective TF analyses in the presence of burst missing samples, the missing data iterative adaptive approach (MIAA) [28] is employed to achieve missing data recovery in the IAF domain under burst missing samples [25]. MIAA is designed to retrieve missing data of stationary signals by utilizing the Capon estimator with a least-squares spectral fitting criterion. The missing data iterative sparse reconstruction (MI-SR) approach [26] extends the work in [25] by utilizing iterative sparse reconstruction procedures, in lieu of the single Capon estimation, to provide more robust and improved TFR reconstruction performance. However, such a grid-based IAF data interpolation procedure inevitably causes a basis mismatch issue [29], when the actual frequencies

This work is supported in part by the National Science Foundation (NSF) under grant AST-1547420.

The authors are with the Department of Electrical and Computer Engineering, Temple University, Philadelphia, PA 19122.

are not aligned on the grid. Another issue with the MI-SR approach is that it does not properly handle signals with weak components which are easily obscured by the residual artifacts induced by the stronger signal components. In [27], an adaptive local filtering-based directional TF distribution is developed to handle multi-component signals with distinct magnitudes in the presence of burst missing samples. This method obtains robust TFR by exploiting local peak detection and filtering within a window around a time instant. However, this method heavily relies on the quality of the kernalized TFR obtained from the incomplete data. It would fail to work if the IFs are seriously misguided by the excessive artifacts.

To address the above-mentioned issues, we recently developed a robust TFR reconstruction method [30] for multi-component FM signals with distinct amplitudes in the presence of burst missing samples. This method is based on the recovery of the IAF missing entries through an atomic norm-based method. This method models an IAF slice, either along the time axis or the lag axis, as the sum of a small number of complex sinusoids in a continuous frequency set, thereby avoiding the basis mismatch issue in IAF interpolation as observed in [26]. Unlike [26] and [27], a TF kernel is applied after performing IAF domain interpolation to suppress cross-terms such that its cross-terms suppression capability is not compromised by the presence of burst missing samples.

It is important to point out that, in all these methods, the IAF interpolation requires a high sparsity of the signal representations in the TF and/or the AF domains, i.e., most of their entries are vacant. While such sparsity requirement is commonly satisfied for auto-terms, cross-terms usually spread over the TF and AF domains before they are effectively mitigated, thus violating this requirement. As a result, the existing methods work well only for certain signals which do not have a high cross-term occupancy in the TF and AF domains, such as mono-component or multi-component parallel linear FM (LFM). On the other hand, their performance significantly degrades for signals with nonlinear FM (NLFM) components or nonparallel FM components whose cross-terms take a high occupancy and thereby invalidate the signal sparsity requirement.

Motivated by this fact, in this paper, we propose a novel approach which can reconstruct the IAF missing entries even in the presence of high-occupancy cross-terms. In this approach, IAF patches are designed to ensure its spectrum in the associated Doppler-frequency (DF) domain to be sparse. IAF patches are then formulated as block Hankel matrices via a partition-and-stacking process, and the annihilating filter-based low-rank Hankel matrix (ALOHA) approach is used to interpolate the IAF and recover missing entries. We then apply the adaptive optimal kernel (AOK) [31] to the interpolated IAF to further mitigate the effects of cross-terms and residual artifacts due to missing samples. Finally, we obtain the high-resolution TFR by implementing sparse reconstruction using orthogonal matching pursuit (OMP) [32]. We refer to the proposed TFR reconstruction method as the AAO (ALOHA+AOK+OMP) method.

The exploitation of IAF patches in the proposed method, instead of using single IAF slices as in [30], offers several

important advantages. First, as cross-terms oscillate with fast phase variation over time [11], whereas auto-terms render positive values around the signal IFs which do not drastically vary within a short time window, concurrently exploiting multiple IAF slices significantly suppresses cross-terms without compromising the auto-term concentrations. Second, applying the patch amounts to placing a window in the IAF domain with respect to lag (similar to the kernel defining the pseudo Wigner-Ville distribution [11]), thus enabling the utilization of moving average to further improve the IAF recovery performance. As a result, the problems encountered by the atomic norm-based approach [30] are effectively eased, particularly for complicated signals with high cross-term occupancy.

The ALOHA approach was originally developed for image inpainting [33], i.e., filling in missing pixels in an image, and has demonstrated its effectiveness in image deconvolution [34], compressed sensing magnetic resonance imaging [35], and binary shape reconstruction from subsampled and blurred images [36]. Within the context of ALOHA, we formulate the problem of IAF recovery as a low-rank block Hankel matrix completion problem. Unlike image inpainting for natural images, where the patch size is chosen by trial and error since the spectral contents of a patch depend on image properties and it is difficult to obtain explicit rules to guide the selection of the patch size [37], the IAF can be analytically represented in the underlying TFR reconstruction problem, and prior information related to the FM signals being processed can be used to optimize the patch size.

The main contributions of this paper are summarized below:

- 1) We develop a novel approach which can reconstruct the IAF missing entries even in the presence of high-occupancy cross-terms.
- 2) By inheriting the advantages of the existing methods, the proposed method avoids the basis mismatch problem and is robust to amplitude differences among multiple signal components.
- 3) We provide theoretical performance analyses for different FM signals. Guided by these results, rules for patch size optimization are provided.

It is noted that the proposed patch-by-patch ALOHA-based IAF recovery method can be considered as a pre-processing method for TFR reconstruction in the presence of missing samples. Therefore, it can be easily implemented in conjunction with other TF kernels (e.g., [38]) and TF filtering techniques (e.g. [39]).

The rest of this paper is structured as follows. Section II describes signal model and demonstrates the effects of burst missing samples. Section III provides a brief introduction of the atomic norm-based TFR reconstruction method in [30]. The proposed robust TFR reconstruction algorithm is described in Section IV. Section V provides simulation results, and finally conclusions are drawn in Section VI.

Notations: Lower-case (upper-case) bold characters are used to denote vectors (matrices). $|\cdot|$ denotes the cardinality of a set. $(\cdot)^*$, $(\cdot)^T$ and $(\cdot)^H$ denote the complex conjugation, transpose and Hermitian transpose, respectively. $\mathcal{F}_x(\cdot)$ and $\mathcal{F}_x^{-1}(\cdot)$ represent the discrete Fourier transform (DFT) and inverse DFT (IDFT) with respect to x , respectively. $\|\cdot\|_*$,

$\|\cdot\|_F$ and $\|\cdot\|_0$ respectively denote the nuclear norm, Frobenius norm, and ℓ_0 -norm. $\lceil \cdot \rceil$ denotes the ceiling function. $\mathcal{T}(\mathbf{x})$ denotes a Hermitian Toeplitz matrix with \mathbf{x} as its first column. $\text{Tr}(\cdot)$ denotes the trace operation.

II. SIGNAL MODEL AND TIME-FREQUENCY REPRESENTATIONS

A. Signal Model

Consider a discrete-time P -component FM signal as

$$s(t) = \sum_{p=1}^P a_p e^{j\phi_p(t)}, t = 1, \dots, T, \quad (1)$$

where a_p and $\phi_p(t)$ respectively denote the amplitude and the phase law of the p th component for $p = 1, \dots, P$. The IF of the p th signal component is expressed as follows:

$$f_p(t) = \frac{1}{2\pi} \frac{d\phi_p(t)}{dt}. \quad (2)$$

In practice, the signal is corrupted by the additive white Gaussian noise $n(t)$, resulting the following noisy signal:

$$x(t) = s(t) + n(t). \quad (3)$$

Denote $r(t)$ as its observation data with L missing data bursts, and $B = \sum_{l=1}^L B_l$ as the total number of missing samples with B_l missing samples in the l th burst, where $0 \leq B_l < T$ for $l = 1, \dots, L$. The bursts of missing samples are randomly distributed over time and do not overlap with each other.

The received signal $r(t)$ can be represented as the product of the noisy signal $x(t)$ and an ‘‘observation mask’’ $m(t)$, i.e.,

$$r(t) = x(t) \cdot m(t), \quad (4)$$

where $m(t)$ is a binary sequence with element 1 for $t \in \mathbb{S}$ and 0 for $t \in \bar{\mathbb{S}}$. Here, $|\mathbb{S}| = T - B$ and $|\bar{\mathbb{S}}| = |\bigcup_{l=1}^L \bar{\mathbb{S}}_l| = B$.

B. Effects of Missing Samples

1) *Instantaneous Autocorrelation Function*: The IAF of the noise-free signal $s(t)$ is defined as [11]

$$R_{ss}(t, \tau) = s(t + \tau) s^*(t - \tau), \quad (5)$$

where τ denotes the time lag.

Following (4), the IAF of $r(t)$ can be formulated as

$$R_{rr}(t, \tau) = R_{xx}(t, \tau) R_{mm}(t, \tau), \quad (6)$$

where $R_{xx}(t, \tau)$ is the IAF of the noisy signal $x(t)$, and $R_{mm}(t, \tau)$ is the IAF of the observation mask $m(t)$. Given

$$\begin{aligned} m(t) &= 1 - \sum_{i=1}^B \delta(t - t_i), t_i \in \bar{\mathbb{S}} \\ &= 1 - \sum_{l=1}^L \sum_{b=1}^{B_l} \delta(t - t_{lb}), t_{lb} \in \bar{\mathbb{S}}_l. \end{aligned} \quad (7)$$

Thus, the IAF of the observation mask is formulated as

$$\begin{aligned} R_{mm}(t, \tau) &= \left[1 - \sum_{i=1}^B \delta(t - t_i + \tau) \right] \left[1 - \sum_{j=1}^B \delta(t - t_j - \tau) \right] \\ &= 1 - R_{mm}^{(1)}(t, \tau) - R_{mm}^{(2)}(t, \tau) + R_{mm}^{(3)}(t, \tau), \end{aligned} \quad (8)$$

where

$$R_{mm}^{(1)}(t, \tau) = \sum_{i=1}^B \sum_{j=1}^T \delta(t - t_j, \tau + t_j - t_i), \quad (9)$$

$$R_{mm}^{(2)}(t, \tau) = \sum_{i=1}^B \sum_{j=1}^T \delta(t - t_j, \tau - t_j + t_i), \quad (10)$$

$$R_{mm}^{(3)}(t, \tau) = \sum_{i=1}^B \sum_{j=1}^B \delta\left(t - \frac{t_i + t_j}{2}, \tau \pm \frac{t_i - t_j}{2}\right). \quad (11)$$

From (8), we observe that missing positions in $r(t)$ are correspondingly linked with the missing IAF entries. Moreover, one missing sample in $r(t)$ results in two intersecting missing diagonal lines in IAF, i.e., $R_{mm}^{(1)}(t, \tau)$ and $R_{mm}^{(2)}(t, \tau)$, which meet at $R_{mm}^{(3)}(t, \tau)$. In the presence of burst missing samples, (9)–(11) can be further expressed as

$$R_{mm}^{(1)}(t, \tau) = \sum_{l=1}^L \left[\sum_{b=1}^{B_l} \sum_{j=1}^T \delta(t - t_j, \tau + t_j - t_{lb}) \right], \quad (12)$$

$$R_{mm}^{(2)}(t, \tau) = \sum_{l=1}^L \left[\sum_{b=1}^{B_l} \sum_{j=1}^T \delta(t - t_j, \tau - t_j - t_{lb}) \right], \quad (13)$$

$$\begin{aligned} R_{mm}^{(3)}(t, \tau) &= \sum_{l_1=1}^L \sum_{l_2=1}^L \sum_{b_1=1}^{B_{l_1}} \sum_{b_2=1}^{B_{l_2}} \\ &\delta\left(t - \frac{t_{l_1 b_1} + t_{l_2 b_2}}{2}, \tau \pm \frac{t_{l_1 b_1} - t_{l_2 b_2}}{2}\right). \end{aligned} \quad (14)$$

Each burst of missing samples will induce two missing IAF strips intersecting at $\tau = 0$. When dealing with a finite data sequence, the IAF has a diamond shape with a time-varying width of $Q = T - |T + 1 - 2t|$ due to the zero-padding effect.

2) *Ambiguity Function*: The AF is the one-dimensional (1-D) DFT of IAF with respect to t , expressed as

$$A_{xx}(\theta, \tau) = \mathcal{F}_t [R_{xx}(t, \tau)] = \sum_t R_{xx}(t, \tau) e^{-j2\pi\theta t}, \quad (15)$$

where θ denotes the frequency shift or Doppler.

In the presence of missing samples, the AF of the partially observed signal $r(t)$ is formulated as

$$\begin{aligned} A_{rr}(\theta, \tau) &= \sum_t R_{xx}(t, \tau) R_{mm}(t, \tau) e^{-j2\pi\theta t} \\ &= A_{xx}(\theta, \tau) + A_D(\theta, \tau), \end{aligned} \quad (16)$$

where $A_D(\theta, \tau) = -A_1(\theta, \tau) - A_2(\theta, \tau) + A_3(\theta, \tau)$ denotes the artifacts caused by missing samples, with

$$A_i(\theta, \tau) = \sum_t R_{xx}(t, \tau) R_{mm}^{(i)}(t, \tau) e^{-j2\pi\theta t}, 1 \leq i \leq 3. \quad (17)$$

3) *Wigner-Ville Distribution*: The Wigner-Ville distribution (WVD) is often referred to as the prototype bilinear TF distribution. The WVD of $x(t)$ can be obtained via the DFT of the IAF $R_{xx}(t, \tau)$ with respect to τ , i.e.,

$$W_{xx}(t, f) = \mathcal{F}_\tau [R_{xx}(t, \tau)] = \sum_\tau R_{xx}(t, \tau) e^{-j4\pi f \tau}. \quad (18)$$

Note here that 4π is used in the DFT instead of 2π to make τ an integer. With missing samples, the resulting WVD is

$$\begin{aligned} W_{rr}(t, f) &= \sum_\tau R_{xx}(t, \tau) R_{mm}(t, \tau) e^{-j4\pi f \tau} \\ &= W_{xx}(t, f) + W_D(t, f), \end{aligned} \quad (19)$$

where $W_D(t, f) = -W_1(t, f) - W_2(t, f) + W_3(t, f)$ denotes the artifacts in the WVD due to the missing data samples, with

$$W_i(\theta, \tau) = \sum_t R_{xx}(t, \tau) R_{mm}^{(i)}(t, \tau) e^{-j4\pi f \tau}, 1 \leq i \leq 3. \quad (20)$$

Even though the WVD is mathematically similar to the AF, we should note that the WVD is real-valued, whereas the AF is complex in general since the IAF is conjugate symmetric only with τ . From (16) and (19), we also notice that each

missing burst in the time domain is analogous to a rectangular function in the time-lag domain, which results in a convolving sinc function applied to both the TF and AF domains.

C. Time-Frequency Kernel

Because of the bilinear nature of WVD, cross-terms are unavoidable for NLFM signals or multi-component signals. It is difficult to obtain an accurate analysis and interpretation of the signal IF signatures with the existence of cross-terms [11]. To address this underlying issue, TF kernels are designed to suppress cross-terms while preserving auto-terms. Essentially, TF kernels are two-dimensional (2-D) filters, which provide low-pass filtering characteristics in the AF domain. They can be classified into two types, i.e., data-independent (fixed) kernels and data-dependent (adaptive) kernels. Popular examples of fixed kernels include the Choi-Williams distribution kernel [40] and the cone kernel [41]. For adaptive kernels, the AOK [31] is commonly used, which is designed based on a radially Gaussian kernel with an angle-dependent size. In general, adaptive kernels provide a better performance, compared to the fixed counterparts since they are optimized based on the signal characteristics.

D. Effects of Amplitude Difference

When the received signal consists of multiple components with different amplitudes, it is much more challenging to retrieve the weaker signal components. Without loss of generality, let us consider a two-component FM signal as follows:

$$s(t) = e^{j\phi_1(t)} + \rho e^{j\phi_2(t)}, \quad (21)$$

where $0 < \rho \leq 1$ is the amplitude ratio. The IAF of the noise-free signal $s(t)$ is

$$R_{ss}(t, \tau) = \underbrace{e^{j[\phi_1(t+\tau) - \phi_1(t-\tau)]} + \rho^2 e^{j[\phi_2(t+\tau) - \phi_2(t-\tau)]}}_{\text{Auto-terms}} + \underbrace{\rho e^{j[\phi_1(t+\tau) - \phi_2(t-\tau)]} + \rho e^{j[\phi_2(t+\tau) - \phi_1(t-\tau)]}}_{\text{Cross-terms}}. \quad (22)$$

Therefore, the average cross-term power is stronger than that of the auto-term associated with the weaker signal component, thus indicating difficulties in recovering the weaker signal component, given that the residual artifacts could be stronger than the auto-terms of the weaker signal component.

E. Demonstration Example

We consider a two-component intersecting LFM signal in a noise-free case. The instantaneous phase laws are given by

$$\begin{aligned} \phi_1(t) &= 2\pi(0.05t + 0.20t^2/T), \\ \phi_2(t) &= 2\pi(0.45t - 0.20t^2/T). \end{aligned} \quad (23)$$

Fig. 1 illustrates the effects of burst missing samples and amplitude difference. 52 out of 128 samples are missing. The first row of Fig. 1 presents the AF, whereas the second row presents the AOK.

Fig. 1(a) and Fig. 1(d) are obtained by the two-component LFM signal with the same amplitude in the presence of random missing samples. We notice that the artifacts in the AF as shown in Fig. 1(a) are distributed evenly. A relative clean TFR is achieved after applying the AOK.

Fig. 1(b) and Fig. 1(e) depict the AF and the AOK under the same amount of missing samples as in the first column of

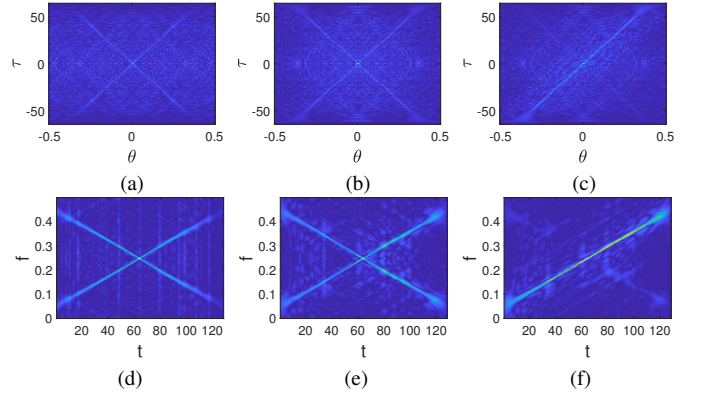


Fig. 1. Comparison of the AF ((a)–(c)) and AOK ((d)–(f)) for the noiseless two-component intersecting LFM signal. (a) and (d) are obtained with the same amplitude ($\rho = 1$) under random missing samples; (b) and (e) are obtained with the same amplitude ($\rho = 1$) under burst missing samples; (c) and (f) are obtained with different amplitudes ($\rho = 0.5$) under burst missing samples.

Fig. 1, but the missing samples occur in bursts, where the 52 missing samples are grouped into 13 bursts, with each burst containing 4 missing samples. Compared to Fig. 1(a), the sinc function artifacts in the AF are highly concentrated near the auto-terms. Fig. 1(e) demonstrates that it is much more difficult to suppress the cross-terms in the presence of burst missing samples. The cross-terms are chunk-like, and the auto-terms are more severely distorted compared to Fig. 1(d), especially when $64 < t < 128$.

Fig. 1(c) and Fig. 1(f) are obtained with the same phase laws and burst missing pattern as in the second column of Fig. 1, but with the amplitude ratio $\rho = 0.5$. Due to the amplitude difference, it is difficult to identify the auto-term associated with the weak signal component from the residual artifacts of the cross-terms, compared with Fig. 1(e).

III. ISSUES IN ATOMIC NORM-BASED IAF RECOVERY

In this section, we first provide a brief summary of atomic norm-based IAF recovery in [30]. Then, its limitations, and the motivations for the proposed method are thoroughly discussed.

A. Atomic norm-based IAF recovery

Let \mathbf{g}_t and \mathbf{y}_t respectively denote the TF slice and the IAF slice at time instant t . P_t non-zero entries in \mathbf{g}_t are considered. The IAF is the IDFT of WVD with respect to f , given by

$$\mathbf{y}_t = \mathcal{F}_f^{-1}(\mathbf{g}_t) = \sum_{p=1}^{P_t} c_t^p e^{j2\pi f_t^p \tau}, \quad (24)$$

where c_t^p denotes the complex amplitude of the p th signal component at time instant t , f_t^p denotes the associated signal frequency, and $\boldsymbol{\tau} = [\tau_1, \dots, \tau_Q]^T$ is the time lag vector. A Hankel matrix constructed from \mathbf{y}_t is expressed as

$$\mathbf{H}_t = \mathcal{H}(\mathbf{y}_t, q_1) = \begin{bmatrix} y_t^1 & y_t^2 & \cdots & y_t^{Q-q_1+1} \\ y_t^2 & y_t^3 & \cdots & y_t^{Q-q_1+2} \\ \vdots & \vdots & \ddots & \vdots \\ y_t^{q_1} & y_t^{q_1+1} & \cdots & y_t^Q \end{bmatrix}, \quad (25)$$

where q_1 is the pencil parameter, which is usually set to $\lceil Q/2 \rceil$. The same P_t frequency components are shared among

all the columns in \mathbf{H}_t . The atom set representing \mathbf{H}_t can be expressed as

$$\mathcal{A} = \left\{ \mathbf{A}(f, \mathbf{b}) = \mathbf{a}(f) \mathbf{b}^H \mid f \in [0, 1), \|\mathbf{b}\|_2 = 1 \right\}. \quad (26)$$

where $\mathbf{A}(f, \mathbf{b})$ denotes one atom, $\mathbf{a}(f) = e^{j2\pi f \boldsymbol{\tau}} \in \mathbb{C}^{q_1}$, for $f \in [0, 1)$, and $\mathbf{b} \in \mathbb{C}^{Q-q_1+1}$ with $\|\mathbf{b}\|_2 = 1$. Here, the basis mismatch issue is avoided since the frequency set is continuously defined. Following the recipe in [42], the atomic norm of \mathbf{H}_t is defined as

$$\begin{aligned} \|\mathbf{H}_t\|_{\mathcal{A}} &= \inf \{ \beta > 0 : \mathbf{H}_t \in \beta \text{conv}(\mathcal{A}) \} \\ &= \inf \left\{ \sum_p |c_t^p| : \mathbf{H}_t = \sum_p |c_t^p| \mathbf{a}(f_t^p, \mathbf{b}_t^p) \right\}, \end{aligned} \quad (27)$$

where $\text{conv}(\mathcal{A})$ is the convex hull of \mathcal{A} .

Denote $\mathbf{z}_t = [R_{rr}(t, \tau_1), \dots, R_{rr}(t, \tau_Q)]^T$ as the t th slice of the IAF of the observed signal $r(t)$, and $\Omega_t = [R_{mm}(t, \tau_1), \dots, R_{mm}(t, \tau_Q)]^T$ as the observation pattern, i.e., the t th IAF slice of the observation mask $m(t)$, and ϵ_t denotes the upper bound of the noise. Then, the recovery of missing entries in the IAF slice \mathbf{y}_t can be formulated into an atomic norm minimization problem as

$$\hat{\mathbf{y}}_t = \arg \min_{\mathbf{y}_t} \|\mathcal{H}(\mathbf{y}_t, q_1)\|_{\mathcal{A}} \quad \text{s.t.} \quad \|\mathbf{y}_t^{\Omega_t} - \mathbf{z}_t^{\Omega_t}\|_2 \leq \epsilon_t. \quad (28)$$

In general, the atomic norm minimization is converted into a semidefinite programming (SDP) [43] problem as follows:

$$\begin{aligned} \min_{\mathbf{u}, \mathbf{W}, \mathbf{y}_t} \quad & \text{Tr}(\mathcal{T}(\mathbf{u})) + \text{Tr}(\mathbf{W}) \\ \text{s.t.} \quad & \begin{bmatrix} \mathcal{T}(\mathbf{u}) & \mathcal{H}(\mathbf{y}_t, q_1) \\ \mathcal{H}(\mathbf{y}_t, q_1)^H & \mathbf{W} \end{bmatrix} \succeq 0, \\ & \|\mathbf{y}_t^{\Omega_t} - \mathbf{z}_t^{\Omega_t}\|_2 \leq \epsilon_t. \end{aligned} \quad (29)$$

The same procedure can be also applied to the IAF slice \mathbf{y}_τ along the lag direction τ , since the AF slice can be viewed sparse and there is a similar DFT relationship between the IAF and the AF according to (15). We denote $\hat{R}_{\text{AT}}(t, \tau)$ as the interpolated IAF via atomic norm-based method. Note that $\hat{R}_{\text{AT}}(t, \tau)$ is referred to as ‘‘stage 1 IAF’’ in [30]. As proved in [43], the missing entries can be recovered with a guarantee under some mild conditions. One key assumption is that P_t should be small.

B. Effects of Cross-Terms on Sparsity

In the existing literatures including [30], the TF domain is assumed to be sparse. However, for bilinear TF analysis, this assumption underestimates the effects of cross-terms. As a result, the performance of [30] degrades dramatically when the signal consists of nonlinear or nonparallel FM signal components. Because in such cases, the cross-terms do not appear as single-frequency components, but span a large region in the TF domain. To demonstrate the impact of cross-terms on the sparsity clearly, without loss of generality, we consider two examples. The first example involves a two-component LFM signal, whereas the second example deals with a two-component NLFM signal for illustration.

1) *Two-Component LFM*: For two-component LFM with different amplitudes, we consider the phase laws as follows:

$$\phi_1(t) = 2\pi (a_1 t + b_1 t^2), \quad \phi_2(t) = 2\pi (a_2 t + b_2 t^2). \quad (30)$$

The IAF of $s(t)$ is

$$\begin{aligned} R_{ss}(t, \tau) &= \underbrace{e^{j2\pi(2a_1+4b_1t)\tau} + \rho^2 e^{j2\pi(2a_2+4b_2t)\tau}}_{\text{Auto-terms}} \\ &\quad + \underbrace{2\rho \cos(2\pi\beta_L) e^{j2\pi(a_1+a_2+2b_1t+2b_2t)\tau}}_{\text{Cross-terms}}, \end{aligned} \quad (31)$$

where $\beta_L = (a_1 - a_2)t + (b_1 - b_2)t^2 + (b_1 - b_2)\tau^2$.

If the two LFM signal components are parallel, i.e., $b_1 = b_2$, then β_L can be simplified to $(a_1 - a_2)t$. Following (31), when t is fixed, the IAF slice \mathbf{y}_t is expressed as

$$\mathbf{y}_t = \sum_{p=1}^{P_t=3} c_t^p e^{j2\pi f_t^p \tau}, \quad (32)$$

where $c_t^1 = 1$, $f_t^1 = 2a_1 + 4b_1t$, $c_t^2 = \rho^2$, $f_t^2 = 2a_2 + 4b_1t$, $c_t^3 = 2\rho \cos(2\pi(a_1 - a_2)t)$, and $f_t^3 = a_1 + a_2 + 4b_1t$.

Similarly, when τ is fixed, the IAF slice \mathbf{y}_τ is expressed as

$$\mathbf{y}_\tau = \sum_{p=1}^{P_\tau=3} c_\tau^p e^{j2\pi f_\tau^p t}, \quad (33)$$

where $c_\tau^1 = e^{j2\pi(2a_1\tau)} + \rho^2 e^{j2\pi(2a_2\tau)}$, $f_\tau^1 = 4b_1\tau$, $c_\tau^2 = \rho e^{j2\pi(a_1+a_2)\tau}$, $f_\tau^2 = a_1 - a_2 + 4b_1\tau$, $c_\tau^3 = \rho e^{j2\pi(a_1+a_2)\tau}$, and $f_\tau^3 = a_2 - a_1 + 4b_1\tau$.

Eqs. (32) and (33) indicate that the IAF with partial observed entries can be recovered via the atomic-norm based approach with a guarantee under mild conditions. However, if $b_1 \neq b_2$, β_L is no longer a constant neither for \mathbf{y}_t nor for \mathbf{y}_τ . In the case of the signal consisting of P non-parallel LFM components, P_t or P_τ is much larger than $2P - 1$, which compromises the sparsity and degrades the performance of the atomic norm-based IAF recovery method [30].

2) *Two-Component NLFM*: For a two-component NLFM signal, we have the phase laws as follows:

$$\begin{aligned} \phi_1(t) &= 2\pi (a_1 + b_1 t^2 + c_1 t^3), \\ \phi_2(t) &= 2\pi (a_2 + b_2 t^2 + c_2 t^3). \end{aligned} \quad (34)$$

The IAF of $s(t)$ is expressed as

$$R_{ss}(t, \tau) = \Delta_1 + \Delta_2 + \Delta_3, \quad (35)$$

where

$$\Delta_1 = e^{j2\pi(2a_1+4b_1t+6c_1t^2)\tau} \cdot e^{j2\pi \cdot 2c_1 \tau^3}, \quad (36)$$

$$\Delta_2 = \rho^2 e^{j2\pi(2a_2+4b_2t+6c_2t^2)\tau} \cdot e^{j2\pi \cdot 2c_2 \tau^3}, \quad (37)$$

$$\begin{aligned} \Delta_3 &= 2\rho \cos(2\pi\beta_{\text{NL}}) e^{j2\pi(c_1+c_2)\tau^3} \\ &\quad \cdot e^{j2\pi(a_1+a_2+2b_1t+2b_2t+3c_1t^2+3c_2t^2)\tau}, \end{aligned} \quad (38)$$

$$\beta_{\text{NL}} = (a_1 - a_2)t + (b_1 - b_2)t^2 + (c_1 - c_2)t^3 + (b_1 - b_2 + 3c_1t - 3c_2t)\tau^2. \quad (39)$$

If the two signal components are parallel, we have $b_1 = b_2$ and $c_1 = c_2$. IAF column \mathbf{y}_t can be expressed as

$$\begin{aligned} \mathbf{y}_t &= e^{j2\pi \cdot 2c_1 \tau^3} \left[e^{j2\pi(2a_1+4b_1t+6c_1t^2)\tau} + \rho^2 e^{j2\pi(2a_2+4b_1t+6c_1t^2)\tau} \right. \\ &\quad \left. + 2\rho \cos(2\pi(a_1 - a_2)t) e^{j2\pi(a_1+a_2+4b_1t+6c_1t^2)\tau} \right] \\ &\triangleq e^{j2\pi \cdot 2c_1 \tau^3} \sum_{p=1}^{P_t=3} c_t^p e^{j2\pi f_t^p \tau}, \end{aligned} \quad (40)$$

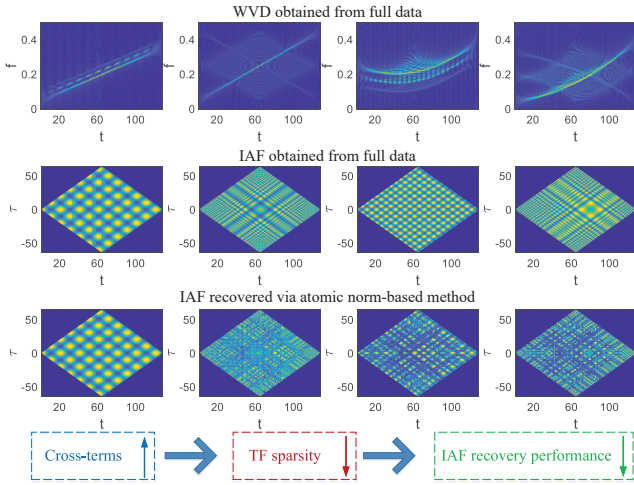


Fig. 2. IAF recovery performance via atomic norm-based method in [30].

whereas IAF row \mathbf{y}_τ can be described as

$$\begin{aligned} \mathbf{y}_\tau &= e^{j2\pi \cdot 2c_1 \tau^3} e^{j2\pi(6c_1 \tau)t^2} \left[e^{j2\pi(4b_1 \tau)t} (e^{j2\pi \cdot 2a_1 \tau} + \rho^2 e^{j2\pi \cdot 2a_2 \tau}) \right. \\ &\quad + \rho e^{j2\pi(a_1 + a_2)\tau} e^{j2\pi(a_1 - a_2 + 4b_1 \tau)t} \\ &\quad \left. + \rho e^{j2\pi(a_1 + a_2)\tau} e^{j2\pi(a_2 - a_1 + 4b_1 \tau)t} \right] \\ &\triangleq e^{j2\pi(6c_1 \tau)t^2} \sum_{p=1}^{P_\tau=3} c_\tau^p e^{2\pi f_\tau^p t}. \end{aligned} \quad (41)$$

We notice that \mathbf{y}_t and \mathbf{y}_τ cannot be described as the sum of only a few complex sinusoidal terms, even though when the two NLFM signal components are parallel. In other words, the spectrum sparsity of \mathbf{y}_t and \mathbf{y}_τ has been greatly compromised by the effects of the cross-terms. Therefore, we can conclude that the atomic norm-based IAF recovery method [30] can achieve a near-optimal recovery performance in the case of the signal containing single or multiple linear parallel FM components in noiseless cases and reconstruct the IAF with a bounded error in noisy environments. However, for the cases including the signal which consists of the NLFM signal component or intersecting FM signal components, the performance will suffer.

Fig. 2 demonstrates the effects of cross-term on TF sparsity, which result in performance degradation of the atomic norm-based IAF interpolation in [30]. For illustration visually, four different kinds of signals are employed (for detailed signal expressions and parameter settings, please refer to Section V-A1–V-A4). All signals have the same observation pattern. As analyzed before, we notice that the atomic norm-based method obtains a near-optimal recovery performance in the case of parallel two-component LFM signal. However, its performance degrades with the increasing cross-terms. Because in the cases of the signal consisting of NLFM or intersecting FM signal components, the resulting cross-terms span a large portion of the TF domain, which prohibit \mathbf{y}_t or \mathbf{y}_τ to be the sum of a small number of complex sinusoids. Therefore, the assumption of atomic norm-based method becomes less valid in such cases.

IV. PROPOSED METHOD

Based on the fact that we can suppress the artifacts due to missing samples by interpolating the associated missing

entries in the IAF, and the effects of cross-terms can be mitigated by using TF kernels, the proposed method aims to improve the IAF estimate such that it is close to the adaptively kernelled IAF obtained from the full data. In this section, we describe the proposed AAO algorithm, which improves the TFR reconstruction performance in detail.

A. IAF Interpolation via Patch-based ALOHA

1) *Ensuring IAF Spectrum Sparsity via Windowing*: A key difference between auto-terms and cross-terms in the TF domain is that cross-terms oscillate with an oscillation frequency being proportional to the distance between corresponding terms, whereas the IFs of an FM signal do not change rapidly over a short time period. By applying the 2-D DFT, the IAF defined in the time-lag domain (t, τ) is converted to the DF domain with a Doppler-frequency pair (θ, f) . The selection of an IAF patch would limit its ranges in time and lag to ensure the spectral sparsity in the DF domain.

Given the spectral sparsity of a small IAF patch, we apply the data interpolation procedure in a patch-by-patch manner. It is equivalent to applying a window function $g(t, \tau)$ in the IAF, which is described as

$$g(t, \tau) = \begin{cases} 1, & \text{if } M_0 + 1 \leq \tau \leq M_0 + M \text{ and} \\ & N_0 + 1 \leq t \leq N_0 + N, \\ 0, & \text{otherwise.} \end{cases} \quad (42)$$

where M_0 and N_0 denote the offsets respectively in the lag direction and time direction, and M and N determine the selected patch size. The IAF patch can be expressed as

$$\mathbf{Y}(M_0, N_0, M, N) = [\mathbf{y}_1, \mathbf{y}_2, \dots, \mathbf{y}_N] \in \mathbb{C}^{M \times N}, \quad (43)$$

with

$$\mathbf{y}_n = [R_{ss}(t_{N_0+n}, \tau_{M_0+1}), \dots, R_{ss}(t_{N_0+n}, \tau_{M_0+M})]^T, \quad (44)$$

for $n \in [1, N]$. For notational convenience, we will abbreviate $\mathbf{Y}(M_0, N_0, M, N)$ as \mathbf{Y} .

The associated spectrum of \mathbf{Y} can be modeled as the sum of 2-D Dirac functions:

$$S(\theta, f) = \sum_{d=1}^D c_d \delta(\theta - \theta_d, f - f_d), \quad (45)$$

where D is the number of non-zero spectral components respectively located at (θ_d, f_d) , $d = 1, \dots, D$. A low value of D is used by properly selecting the patch size defined by M and N and will be discussed in Section IV-A(2).

Given (45), it is clear that there is a corresponding annihilating filter [44] in the time-lag domain which leads to

$$h(\theta, f)S(\theta, f) = 0. \quad (46)$$

Note here that, the underlying frequencies of the IAF patch are not restricted on the grid and can assume any continuous values in the normalized frequency domain such that the basis mismatch issue is avoided just as [30]. We recall a result that there is a fundamental duality between the sparsity in the primary space and the low-rankness of a structured matrix in the corresponding spectral domain. We construct the following block Hankel matrix \mathbf{H} with pencil parameters k_1, k_2 , from the IAF entries within the patch \mathbf{Y} :

TABLE I
NUMERICAL RANK COMPARISON OF BLOCK HANKEL MATRIX FOR DIFFERENT TWO-COMPONENT PARALLEL LFM SIGNALS

m	Δf_0	Auto	Cross	Auto+cross	CR%
0.002	0.05	2	2	4	2.37%
	0.10	2	2	4	2.37%
	0.15	2	2	4	2.37%
0.02	0.05	6	6	9	5.33%
	0.10	6	6	12	7.10%
	0.15	6	6	12	7.10%
0.2	0.05	13	13	16	9.47%
	0.10	16	16	26	15.38%
	0.15	16	16	30	17.75%
0.4	0.05	20	20	22	13.02%
	0.10	25	25	34	20.12%
	0.15	28	28	46	27.22%

TABLE II
NUMERICAL RANK COMPARISON OF BLOCK HANKEL MATRIX FOR THE PARALLEL TWO-COMPONENT LFM SIGNAL AND THE INTERSECTING TWO-COMPONENT LFM SIGNAL

	m	Δf_0	Auto	Cross	Auto+cross	CR%
Parallel	0.1	0.1	12	12	21	12.43%
Intersecting			12	12	16	9.47%
Parallel	0.15	0.15	14	14	27	13.61%
Intersecting			14	14	23	13.61%
Parallel	0.2	0.2	16	16	32	18.93%
Intersecting			16	16	31	18.34%
Parallel	0.25	0.25	18	18	36	21.30%
Intersecting			20	20	38	22.49%

$$\begin{aligned}
 \mathbf{H} &= \mathcal{H}(\mathbf{Y}, k_1, k_2) \\
 &= \begin{bmatrix} \mathcal{H}(\mathbf{y}_1, k_1) & \mathcal{H}(\mathbf{y}_2, k_1) & \cdots & \mathcal{H}(\mathbf{y}_{N-k_2+1}, k_1) \\ \mathcal{H}(\mathbf{y}_2, k_1) & \mathcal{H}(\mathbf{y}_3, k_1) & \cdots & \mathcal{H}(\mathbf{y}_{N-k_2+2}, k_1) \\ \vdots & \vdots & \ddots & \vdots \\ \mathcal{H}(\mathbf{y}_{k_2}, k_1) & \mathcal{H}(\mathbf{y}_{k_2+1}, k_1) & \cdots & \mathcal{H}(\mathbf{y}_N, k_1) \end{bmatrix} \quad (47) \\
 &\in \mathbb{C}^{k_1 k_2 \times (M-k_1+1)(N-k_2+1)},
 \end{aligned}$$

where $\mathcal{H}(\mathbf{y}_n, k_1) \in \mathbb{C}^{k_1 \times (M-k_1+1)}$ is a Hankel matrix as defined in (25) for $n = 1, \dots, N$. The rank of the block Hankel matrix constructing from \mathbf{Y} is at most D [45], [46].

2) *Patch Size Selection*: In principle, the patch size parameters M and N should be chosen to ensure the sparsity of the spectrum of the IAF patch. It is usual to choose $M = N$ to make the block Hankel matrix as square as possible [47]. However, it is noted that the spectral sparsity of the IAF patch is less sensitive to the selection of M than N since, for each IAF slice \mathbf{y}_t , the frequency components do not change.

For illustration, we consider a two-component parallel LFM signal in which only two variables, i.e., frequency slope m and the initial frequency difference Δf_0 , are involved. The instant frequencies are described as:

$$f_1(t) = 0.05 + mt/T, \quad f_2(t) = 0.05 + \Delta f_0 + mt/T. \quad (48)$$

Due to the duality between the IAF spectrum sparsity and the low rankness of the block Hankel matrix, we choose the numerical rank to examine the effectiveness of cross-term mitigation via the patch-based manner. The numerical rank is calculated as the number of singular values above 0.5%

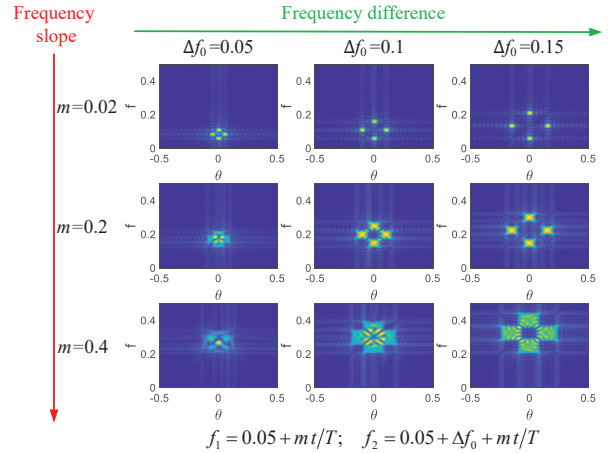


Fig. 3. DF obtained from the IAF patch.

of the maximum singular value for the block Hankel matrix $\mathcal{H}(\mathbf{Y}, k_1, k_2)$. The compressive ratio CR% is defined as

$$\text{CR}\% = \frac{\text{numerical rank}}{\min(k_1 k_2, (M-k_1+1)(N-k_2+1))} \times 100\%. \quad (49)$$

For fair comparison, the same patch size 27×27 with pencil parameters $k_1 = k_2 = 15$ is adopted throughout the paper, and the resulting dimension of the block Hankel matrix is 225×169 .

The numerical rank comparisons with different frequency slopes m and frequency differences Δf_0 are presented in Table I. The formulas for auto-terms and cross-terms can take (31) as a reference. It is observed that the rank generally increases when frequency slope m and difference Δf_0 increase. Interestingly, the auto-terms and cross-terms lead to the same rank, if we check the block Hankel matrix generating from the auto-terms and cross-terms individually. The impacts of cross-terms are mitigated more when the two components are closer.

Fig. 3 compares the DF obtained from the IAF patch for signals listed in Table I. Each column represents the same frequency difference with different frequency slopes, whereas each row represents the same frequency slope with different frequency differences. We notice that slope m makes a greater impact than the frequency difference between the two components, regarding the spectral sparsity of the IAF patch. When the slope is large, the effects of frequency difference become more pronounced. A small frequency difference can help to obtain a sparse DF from the IAF patch.

For the atomic-norm based IAF interpolation method [30], the interpolation performance severely degrades when the signal components are not parallel since, in such cases, the effects of cross-terms become more pronounced. Selecting an IAF patch, however, amounts to windowing the IAF domain to render its DF domain representation to be sparse. Therefore, having parallel IF signatures is not a key factor in the proposed method. We illustrate this by comparing the numerical rank between a two-component parallel LFM signal $s_1(t)$ and a two-component intersecting LFM signal $s_2(t)$. $s_1(t)$ consists of IFs $f_1(t)$ and $f_2(t)$ as described in (48), and $s_2(t)$ consists of IFs $f_1(t)$ and $f_3(t)$, where $f_3(t) = 0.05 + m - mt/T$. Table II provides the numerical rank comparison between the two-component parallel LFM signal $s_1(t)$ and the two-component intersecting LFM signal $s_2(t)$. We notice that the performance

of the proposed method does not degrade when the two LFM signal components have intersecting IFs.

The frequency span in the DF domain along the f direction is equivalent to the one in the TF domain. Similarly, the frequency span in the DF domain along the θ direction is equivalent to the one in the AF domain. For a desired patch size, the frequency span along both the f and θ directions should be kept small. Let $f_{\text{DR}}^p = f_{\text{max}}^p - f_{\text{min}}^p$ denote the dynamic frequency range for the p th signal component and $\Delta f_{\text{max}}^{p,q} = f_{\text{max}}^p - f_{\text{max}}^q$ the maximum frequency difference between the p th signal component and the q th signal component in the patch for $1 \leq p, q \leq P$. Here, we provide a rule of thumb to select a suitable patch size,

$$f_{\text{DR}}(1 + f_{\text{DR}})^{100\Delta f} \leq \eta, \quad (50)$$

where $\Delta f = \max([\Delta f_{\text{max}}^{1,2}, \dots, \Delta f_{\text{max}}^{p,q}, \dots, \Delta f_{\text{max}}^{1,P}])$, $f_{\text{DR}} = \max([f_{\text{DR}}^1, \dots, f_{\text{DR}}^P])$, and η denotes a threshold value. For the two-component parallel LFM, $f_{\text{DR}} = mNt/T$, and a typical value for η is 0.3. In summary, the variation of the IFs should be kept small in the selected patch.

3) *ALOHA Implementation*: To achieve an IAF estimate as close to $R_{ss}(t, \tau)$, i.e., the IAF obtained from the full data of the noise-free signal $s(t)$, we need to suppress not only the artifacts introduced by the missing samples but also the effects of additive noise. Denote $\mathbf{Z} \in \mathbb{C}^{M \times N}$ as a patch of IAF \mathbf{R}_{rr} obtained using the incomplete and noisy data. An interpolated and denoised IAF is obtained by solving the following low-rank Hankel matrix completion problem:

$$\begin{aligned} \min \quad & \text{rank}(\mathcal{H}(\mathbf{Y}, k_1, k_2)) \\ \text{s.t.} \quad & \|\mathbf{Y}_\Omega - \mathbf{Z}_\Omega\|_F^2 \leq \varepsilon, \end{aligned} \quad (51)$$

where Ω denotes the observation pattern within the associated IAF patch of the observation mask $m(t) \in \mathbb{R}^{M \times N}$, and ε is a constant determined by the noise level. Because the optimization problem of (51) is NP-hard, we relax the rank constraint in (51) by utilizing the nuclear norm instead [48]:

$$\|\mathcal{H}(\mathbf{Y}, k_1, k_2)\|_* = \min_{\mathbf{U}, \mathbf{V}: \mathcal{H}(\mathbf{Y}, k_1, k_2) = \mathbf{U}\mathbf{V}^H} \|\mathbf{U}\|_F^2 + \|\mathbf{V}\|_F^2. \quad (52)$$

Therefore, problem (51) is reformulated as

$$\begin{aligned} \min_{\mathbf{Y}} \quad & \|\mathbf{U}\|_F^2 + \|\mathbf{V}\|_F^2 \\ \text{s.t.} \quad & \|\mathbf{Y}_\Omega - \mathbf{Z}_\Omega\|_F^2 \leq \varepsilon, \\ & \mathcal{H}(\mathbf{Y}, k_1, k_2) = \mathbf{U}\mathbf{V}^H. \end{aligned} \quad (53)$$

The augmented Lagrangian form of (53) is formulated as

$$\begin{aligned} L(\mathbf{U}, \mathbf{V}, \mathbf{Y}, \boldsymbol{\Lambda}) := & \frac{\lambda}{2} \|\mathbf{Y}_\Omega - \mathbf{Z}_\Omega\|_F^2 + \frac{1}{2} (\|\mathbf{U}\|_F^2 + \|\mathbf{V}\|_F^2) \\ & + \frac{\mu}{2} \left\| \mathcal{H}(\mathbf{Y}, k_1, k_2) - \mathbf{U}\mathbf{V}^H + \boldsymbol{\Lambda} \right\|_F^2, \end{aligned} \quad (54)$$

where λ and μ are the regularization parameters.

The block Hankel structure increases the matrix dimension and memory requirements, while retaining the intrinsic low-rank property. To reduce the computational complexity, problem (54) is solved using an alternating direction method of multipliers (ADMM)-based technique [49]. More specifically, $\mathbf{Y}^{(i+1)}$, $\mathbf{U}^{(i+1)}$, $\mathbf{V}^{(i+1)}$, and the Lagrangian update $\boldsymbol{\Lambda}^{(i+1)}$ at

the $(i+1)$ th iteration are sequentially updated by solving the following optimization problems:

$$\begin{aligned} \mathbf{Y}^{(i+1)} = & \arg \min_{\mathbf{Y}} \frac{\lambda}{2} \|\mathbf{Y}_\Omega - \mathbf{Z}_\Omega\|_F^2 \\ & + \frac{\mu}{2} \|\mathcal{H}(\mathbf{Y}, k_1, k_2) - \mathbf{U}^{(i)}(\mathbf{V}^{(i)})^H + \boldsymbol{\Lambda}^{(i)}\|_F^2, \end{aligned} \quad (55)$$

$$\begin{aligned} \mathbf{U}^{(i+1)} = & \arg \min_{\mathbf{U}} \frac{1}{2} \|\mathbf{U}\|_F^2 \\ & + \frac{\mu}{2} \|\mathcal{H}(\mathbf{Y}^{(i+1)}, k_1, k_2) - \mathbf{U}(\mathbf{V}^{(i)})^H + \boldsymbol{\Lambda}^{(i)}\|_F^2, \end{aligned} \quad (56)$$

$$\begin{aligned} \mathbf{V}^{(i+1)} = & \arg \min_{\mathbf{V}} \frac{1}{2} \|\mathbf{V}\|_F^2 \\ & + \frac{\mu}{2} \|\mathcal{H}(\mathbf{Y}^{(i+1)}, k_1, k_2) - \mathbf{U}^{(i+1)}\mathbf{V}^H + \boldsymbol{\Lambda}^{(i)}\|_F^2, \end{aligned} \quad (57)$$

$$\boldsymbol{\Lambda}^{(i+1)} = \mathcal{H}(\mathbf{Y}^{(i+1)}, k_1, k_2) - \mathbf{U}^{(i+1)}(\mathbf{V}^{(i+1)})^H + \boldsymbol{\Lambda}^{(i)}. \quad (58)$$

Eqs. (56) and (57) can be easily computed by taking the derivative with respect to \mathbf{U} and \mathbf{V} , leading to the following closed-form update equations:

$$\begin{aligned} \mathbf{U}^{(i+1)} = & \mu(\mathcal{H}(\mathbf{Y}^{(i+1)}, k_1, k_2) + \boldsymbol{\Lambda}^{(i)}) \\ & \cdot \mathbf{V}^{(i)}(\mathbf{I} + \mu(\mathbf{V}^{(i)})^H\mathbf{V}^{(i)})^{-1}, \end{aligned} \quad (59)$$

$$\begin{aligned} \mathbf{V}^{(i+1)} = & \mu(\mathcal{H}(\mathbf{Y}^{(i+1)}, k_1, k_2) + \boldsymbol{\Lambda}^{(i)})^H\mathbf{U}^{(i+1)} \\ & \cdot (\mathbf{I} + \mu\mathbf{U}^{(i+1)H}(\mathbf{U}^{(i+1)})^H)^{-1}. \end{aligned} \quad (60)$$

We utilize a low-rank factorization model (LMaFit) algorithm [50] to initialize \mathbf{U} and \mathbf{V} , which is singular value decomposition-free, so that the computation burden is further reduced.

In this paper, we average the estimated values of overlapping patches in case of the boundary discontinuity among patches. The reconstructed IAF exploiting the patch-by-patch ALOHA-based method is referred to as ‘‘stage 1 IAF’’ $\hat{R}_{rr}^{(1)}(t, \tau)$.

For the underlying low-rank structured matrix completion problem, the Hermitian symmetry property of the IAF is used to further reduce the computational complexity. Let $\hat{\mathbf{y}}_t$ denote the IAF entries of $\hat{R}_{rr}^{(1)}(t, \tau)$ along the τ dimension at time instant t . $\hat{\mathbf{y}}_t$ has a Hermitian symmetric structure, given as

$$\hat{\mathbf{y}}_t = \left[\hat{y}_t^1, \dots, \hat{y}_t^{I-1}, \hat{y}_t^I, (\hat{y}_t^{I-1})^*, \dots, (\hat{y}_t^1)^* \right]^T, \quad (61)$$

where I is the index of the central element in τ . As such, the computational complexity is reduced to the half since we only need to recover half of the IAF with missing samples.

The low-rank matrix completion performance is decided by the incoherence condition, which depends only on the frequency locations regardless of the amplitudes of their respective coefficients. Therefore, the ALOHA-based IAF interpolation method is robust to amplitude differences among different signal components.

B. Cross-term Mitigation via Kerneled IAF

Because the IAF interpolation cannot suppress cross-terms which exist even in absence of the missing samples, we use the AOK, a signal-adaptive kernel, denoted in the AF domain as $\Psi(\theta, \tau)$, and obtain the interpolated and kerneled IAF as

$$\hat{R}_{rr}^{(2)}(t, \tau) = \mathcal{F}_\theta^{-1} \left[\mathcal{F}_t(\hat{R}_{rr}^{(1)}(t, \tau))\Psi(\theta, \tau) \right]. \quad (62)$$

The use of AOK can further mitigate the effects of missing samples as well as noise. The resulting ‘‘stage 2 IAF’’

$\hat{R}_{rr}^{(2)}(t, \tau)$ is expected to be close to the keneled IAF obtained using the full data in a noise-free case. Note that, the interpolated IAF $\hat{R}_{rr}^{(1)}$ can also be used in conjunction with any other kernels such as the adaptive directional TF distribution (ADTFD) [38] and multi-directional distribution (MDD) [9].

C. Sparse Reconstruction of Time-Frequency Representation

After successful suppression of artifacts due to missing samples, cross-terms and reduction of noise, the TFR reconstruction can be viewed as a sparse reconstruction problem by utilizing the sparsity of the FM signals in the TF domain [20], [26], [51]. The non-zero entries of \mathbf{g}_t can be estimated by

$$\hat{\mathbf{g}}_t = \arg \min_{\mathbf{g}_t} \|\mathbf{g}_t\|_1 \quad \text{s.t.} \quad \hat{\mathbf{y}}_t = \Phi \mathbf{g}_t, \quad \forall t, \quad (63)$$

where Φ denotes the IDFT dictionary matrix. Commonly used compressive sensing techniques, such as the OMP [32], and least absolute shrinkage and selection operator (LASSO) [52], can be used to solve problem (63). In this paper, OMP is chosen since it allows us to specify the sparsity at each time instant t .

It is noted that, applying a TF kernel widens the auto-term ridges due to the width and the non-rectangular shape of the kernel. Therefore, for a P -component signal, the occupancy at each time instant t is several-fold higher than P . As such, when the OMP method is used, the sparsity used for sparse reconstruction should be higher than the actual number of signal components, P , to ensure proper recovery of the weak signal component.

D. Computational Complexity Analysis

The computational complexity of ADMM implementation is mainly determined by the matrix inversions in (59) and (60). More specifically, each matrix inversion involves $\mathcal{O}(M - k_1 + 1)(N - k_2 + 1)k_1k_2D + D^3$ multiplications. For (58), the required number of multiplications is $\mathcal{O}(M - k_1 + 1)(N - k_2 + 1)k_1k_2D$. Denote J as the number of output frequency samples for AOK at each time constant. The computational cost of the AOK is $\mathcal{O}(TJ^2)$. For sparse reconstruction, the computation cost of the OMP is $\mathcal{O}(KT^2)$, where K is the defined sparsity. It is usual to take the value of K slightly higher than P for a P -component with distinct amplitudes since the resolution of auto-terms is comprised due to the mitigation of cross-terms.

V. SIMULATION RESULTS

To demonstrate the effectiveness of the proposed method, we consider both synthetic and real-world signals. For synthetic signals, we adopt two-component FM signals with distinct amplitudes, expressed as:

$$x(t) = e^{j\phi_1(t)} + 0.5e^{j\phi_2(t)}, \quad (64)$$

where different forms of $\phi_1(t)$ and $\phi_2(t)$ are considered. For real-world signals, we consider measured new-born electroencephalogram seizure signal and bat echolocation signal.

Unless otherwise specified, we assume $T = 128$ and each missing burst contains 4 missing entries. 52 samples are missing in total and no noise is considered. The default patch size is 27×27 , and the pencil parameters are chosen as $k_1 = k_2 = 15$, resulting in $\mathcal{H}(\mathbf{Y}, k_1, k_2) \in \mathbb{C}^{225 \times 169}$. 50 iterations are used for the ADMM. For LMFit, the initial

rank used in the increasing strategy is one and the tolerance is 1.25×10^{-4} . For the two-component signals being considered in this paper, the sparsity is empirically chosen between 14 to 20.

A. Case Studies

1) *Two-Component Parallel LFM Signal*: The instantaneous phase laws of the two components are respectively given as:

$$\begin{aligned} \phi_1(t) &= 2\pi(0.05t + 0.15t^2/T), \\ \phi_2(t) &= 2\pi(0.10t + 0.15t^2/T). \end{aligned} \quad (65)$$

As a baseline, we first show respectively in Figs. 4(a) and 4(b) the IAF and WVD when all data samples are observed without missing samples. The IAF demonstrates a periodic structure since the frequency difference between the two signal components is a constant. When missing samples are present, the missing entries in the IAF are clearly seen in Fig. 4(c) and cause strong artifacts scattered around the signal IFs as shown in Fig. 4(d). In Fig. 4(e), the TFR is obtained from the keneled IAF using the AOK, with substantial improvement but residual artifacts remain. Fig. 4(f) shows the sparsely reconstructed TFR of Fig. 4(e) via OMP. We notice further improvement with remaining artifacts around the true IFs.

Fig. 4(g) depicts the IAF after atomic norm-based interpolation [30]. Compared to Fig. 4(c), the result is very close to the full IAF shown in Fig. 4(a). The final TFR obtained by [30] is shown in Fig. 4(h), where the weak signal component is clearly recovered.

Figs. 4(i) and 4(j) show the well recovered IAF and WVD via the patch-based ALOHA method. Fig. 4(k) shows that the use of AOK substantially mitigates the cross-terms, yielding a clean TFR. Finally, applying the OMP yields a high-resolution TFR with a high fidelity, as shown in Fig. 4(l), where the weaker component is clearly detected. Comparison to Fig. 4(h) obtained using the method in [30], the proposed AAO method provides a smoother TFR, especially at the two ends.

It is noted that the colorbar depicted in Fig. 4 is scaled by the maximum value of the corresponding figure and applies to all plots in Fig. 5 through Fig. 10.

2) *Two-Component Intersecting LFM Signal*: In this case, the instantaneous phase laws of the two components are described in (23).

Fig. 5 shows the results for this signal. Compared to the parallel LFM case depicted in Fig. 4, the IAF in Fig. 5(a) does not have a periodic structure because the frequency difference between the two signal components varies with the time, and the cross-terms have a higher presence and are more difficult to be suppressed as indicated in Fig. 5(f). In this case, we cannot detect the weak signal component, even after the application of the AOK and OMP.

As analyzed in Section III-B2, the atomic norm-based IAF recovery method [30] does not offer a satisfactory performance in such a challenging case with intersecting signals due to strong cross-terms. As shown in Fig. 5(g), it fails to fill in the missing entries of the IAF properly. In Fig. 5(h), we observe that only the strong signal component is detected in the resulting TFR obtained by [30].

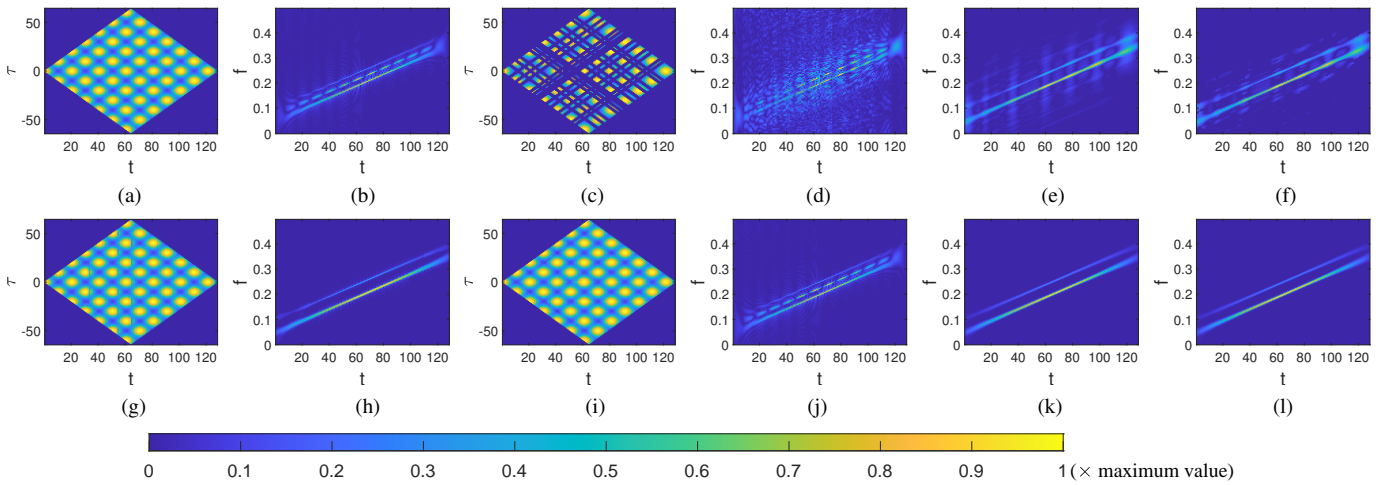


Fig. 4. Results for a noiseless two-component parallel LFM signal. (a) IAF in the absence of missing samples; (b) WVD in the absence of missing samples; (c) IAF with burst missing samples; (d) WVD with burst missing samples; (e) TFR using AOK with burst missing samples; (f) TFR using AOK and OMP with burst missing samples; (g) IAF recovered by atomic norm [30]; (h) TFR proposed in [30]; (i) IAF for stage 1 (patch-based ALOHA); (j) WVD for stage 1 (patch-based ALOHA) (k) TFR for stage 2 (patch based ALOHA + AOK); (l) The proposed AAO TFR (patch-based ALOHA + AOK + OMP).

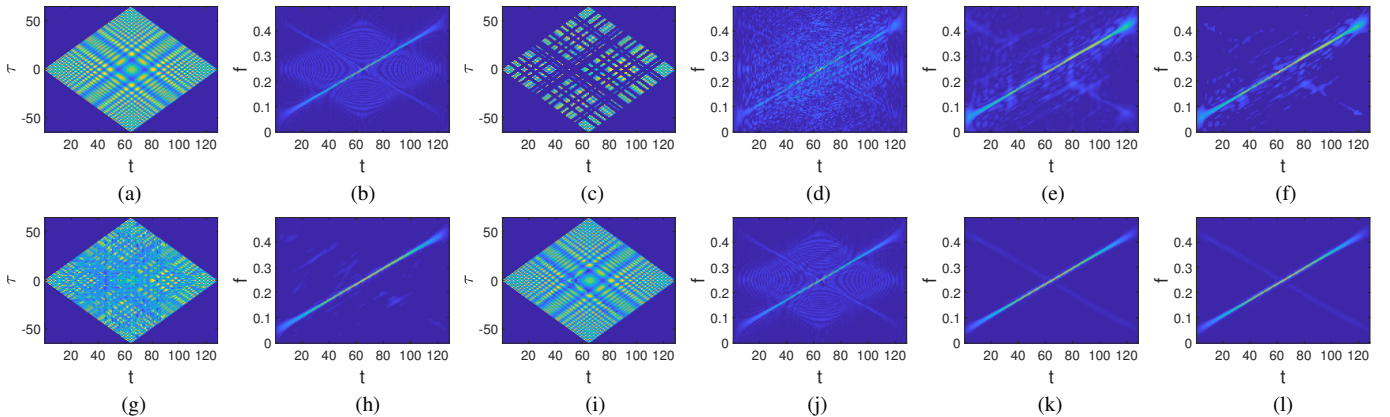


Fig. 5. Results for a noiseless two-component intersected LFM signal. (a) IAF in the absence of missing samples; (b) WVD in the absence of missing samples; (c) IAF with burst missing samples; (d) WVD with burst missing samples; (e) TFR using AOK with burst missing samples; (f) TFR using AOK and OMP with burst missing samples; (g) IAF recovered by atomic norm [30]; (h) TFR proposed in [30]; (i) IAF for stage 1 (patch-based ALOHA); (j) WVD for stage 1 (patch-based ALOHA) (k) TFR for stage 2 (patch based ALOHA + AOK); (l) The proposed AAO TFR (patch-based ALOHA + AOK + OMP).

Figs. 5(i) and 5(j) respectively present the IAF and the corresponding WVD obtained using the patch-based ALOHA method. The results are very close to the baseline IAF and WVD as shown in Figs. 5(a) and 5(b). The TFR, after further using the AOK, is shown in Fig. 5(k). Fig. 5(l) shows the final TFR obtained through sparse reconstruction using OMP. The signal IFs both can be clearly identified in Figs. 5(k) and 5(l). This result aligns with the conclusion observed in Table II and further confirms that the proposed ALOHA-based IAF recovery method is insensitive to the effect of complicated cross-terms due to the signal components with intersecting IF signatures. This represents one of the key advantages of the proposed method over [30].

3) *Two-component Parallel NLFM Signal*: The instantaneous phase laws of the two components are given as:

$$\begin{aligned}\phi_1(t) &= 2\pi \left(0.25t - 0.15t^2/T + 0.15t^3/T^2 \right), \\ \phi_2(t) &= 2\pi \left(0.15t - 0.15t^2/T + 0.15t^3/T^2 \right).\end{aligned}\quad (66)$$

The baseline IAF and WVD without missing samples are shown in Figs. 6(a) and 6(b). Similar to the case of a two-component parallel LFM signal, the IAF also demonstrates a

periodic structure. However, cross-terms are more prominent since the nonlinearity of the IF laws contributes to the cross-terms. Thus, it is difficult to recover the IFs faithfully, as shown in Fig. 6(f), even with the utilization of AOK and OMP.

The atomic norm-based IAF recovery method mitigates the effects of the burst missing samples to some extent in this case, as shown in Fig. 6(g). While the TFR showing in Fig. 6(h) provides some improvement from Fig. 6(f), the weak signal component still cannot be clearly observed.

Figs. 6(i) and 6(j) show the IAF and WVD reconstructed by the proposed ALOHA-based method. All missing entries of the IAF are properly recovered, and the effects of the burst missing samples are effectively mitigated. The TFR after applying AOK and its corresponding sparse reconstruction result using OMP are presented in Fig. 6(k) and Fig. 6(l), respectively. We observe that, in this case, the proposed method provides desirable TFR reconstruction performance, which is not affected by the nonlinearity of the IF laws.

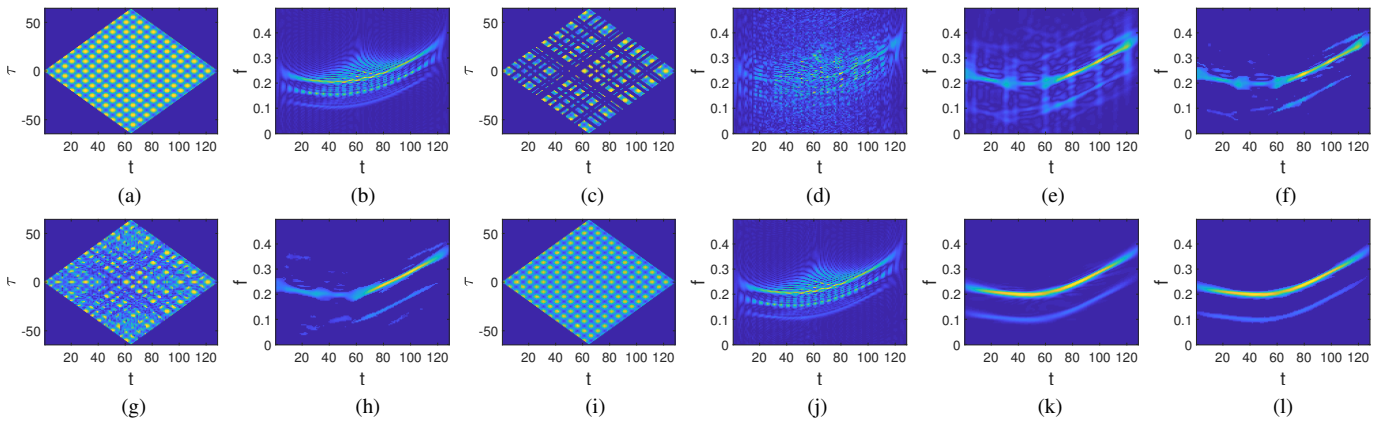


Fig. 6. Results for a noiseless two-component parallel NLFM signal. (a) IAF in the absence of missing samples; (b) WVD in the absence of missing samples; (c) IAF with burst missing samples; (d) WVD with burst missing samples; (e) TFR using AOK with burst missing samples; (f) TFR using AOK and OMP with burst missing samples; (g) IAF recovered by atomic norm [30]; (h) TFR proposed in [30]; (i) IAF for stage 1 (patch-based ALOHA); (j) WVD for stage 1 (patch-based ALOHA); (k) TFR for stage 2 (patch based ALOHA + AOK); (l) The proposed AAO TFR (patch-based ALOHA + AOK + OMP).

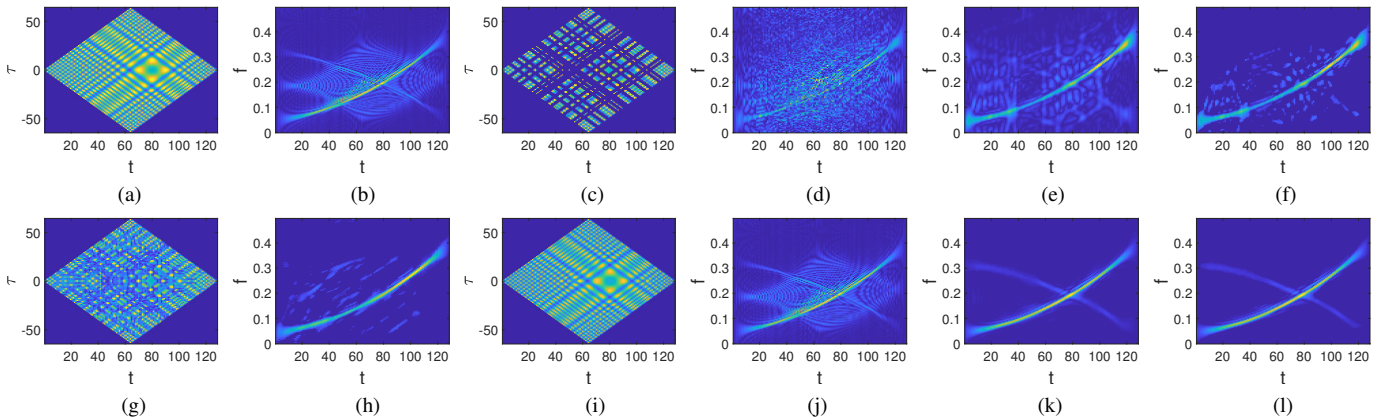


Fig. 7. Results for a noiseless two-component intersected NLFM signal. (a) IAF in the absence of missing samples; (b) WVD in the absence of missing samples; (c) IAF with burst missing samples; (d) WVD with burst missing samples; (e) TFR using AOK with burst missing samples; (f) TFR using AOK and OMP with burst missing samples; (g) IAF recovered by atomic norm [30]; (h) TFR proposed in [30]; (i) IAF for stage 1 (patch-based ALOHA); (j) WVD for stage 1 (patch-based ALOHA); (k) TFR for stage 2 (patch based ALOHA + AOK); (l) The proposed AAO TFR (patch-based ALOHA + AOK + OMP).

4) *Two-Component Intersecting NLFM Signal*: The instantaneous phase laws of the two components are given as:

$$\begin{aligned}\phi_1(t) &= 2\pi (0.05t + 0.025t^2/T + 0.10t^3/T^2), \\ \phi_2(t) &= 2\pi (0.32t - 0.035t^2/T - 0.07t^3/T^2).\end{aligned}\quad (67)$$

Fig. 7 shows the results in this case. The baseline IAF and the corresponding WVD in the absence of missing samples are respectively shown in Figs. 7(a) and 7(b). Figs. 7(c) and 7(d) respectively show the IAF and the WVD in the presence of burst missing samples. Similar to the case of the two-component intersecting LFM signal in Section V-A2, the weak signal component is difficult to be detected after applying the AOK and OMP, as indicated by Figs. 7(e) and 7(f).

The IAF recovered via the atomic norm-based method is presented in Fig. 7(g), which shows the IAF is not properly recovered. The weak signal component is not detected in the obtained TFR, as shown in Fig. 7(h).

Fig. 7(i) shows the recovered IAF via the proposed ALOHA-based method, where most of the missing entries are successfully recovered. As shown in Fig. 7(j), the resulting WVD is very close to the baseline WVD obtained without missing samples. The effects of cross-terms are effectively mitigated after further applying the AOK, as shown in Fig. 7(k). The sparse reconstruction results are shown in Fig. 7(l)

with a high fidelity. As such, the proposed AAO method successfully reconstructs the TFR with clear IF signatures.

5) *Sinusoidal FM and LFM Signal*: In this case, the instantaneous phase laws of the two components are as follows:

$$\begin{aligned}\phi_1(t) &= 2\pi (T/20\pi \cos(2\pi t/T + \pi) + 0.25t), \\ \phi_2(t) &= 2\pi (0.07t + 0.20t^2/T).\end{aligned}\quad (68)$$

The baseline IAF and WVD in the absence of missing samples are shown in Figs. 8(a) and 8(b), respectively. The IAF with burst missing samples and the corresponding WVD are respectively presented in Figs. 8(c) and 8(d). Compared to the previous four cases, this case consisting of a sinusoidal FM and a LFM signal is much more challenging because of the rapid frequency variation of the former and the complicated cross-terms. The TFR obtained after applying the AOK and OMP, as shown in Fig. 8(f), does not clearly recognize the strong signal component, not to mention the weak one.

The atomic norm-based IAF and the resulting TFR are depicted in Figs. 8(g) and 8(h), respectively. By mitigating the effects of burst missing samples, the strong sinusoidal FM component can be better recognized, but the weak LFM signal component remains not clear.

Fig. 8(i) shows the interpolated IAF via the proposed ALOHA-based method, which is close to the baseline IAF and

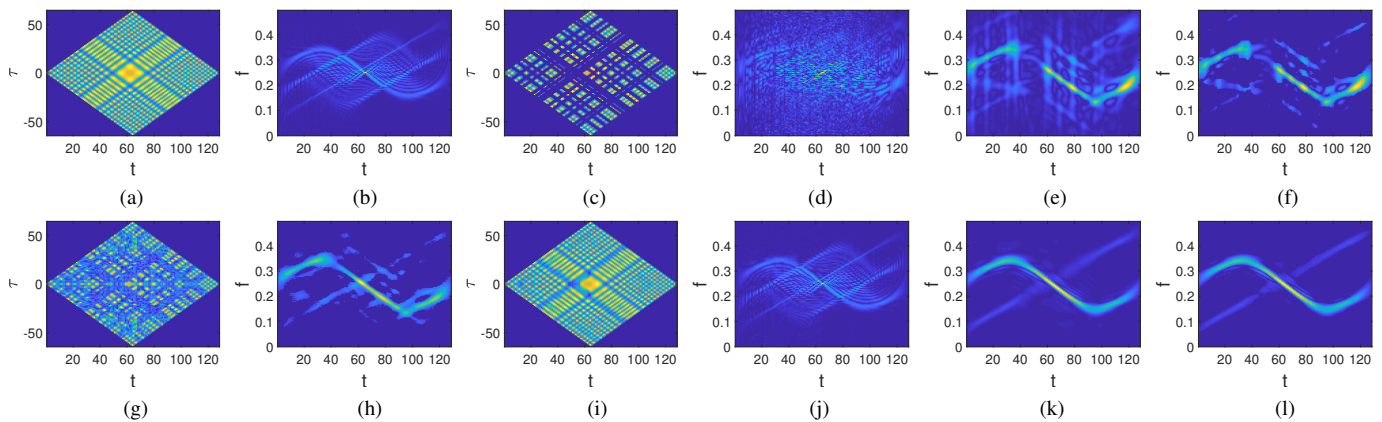


Fig. 8. Results for a noiseless sinusoidal FM and LFM. (a) IAF in the absence of missing samples; (b) WVD in the absence of missing samples; (c) IAF with burst missing samples; (d) WVD with burst missing samples; (e) TFR using AOK with burst missing samples; (f) TFR using AOK and OMP with burst missing samples; (g) IAF recovered by atomic norm [30]; (h) TFR proposed in [30]; (i) IAF for stage 1 (patch-based ALOHA); (j) WVD for stage 1 (patch-based ALOHA) (k) TFR for stage 2 (patch based ALOHA + AOK); (l) The proposed AAO TFR (patch-based ALOHA + AOK + OMP).

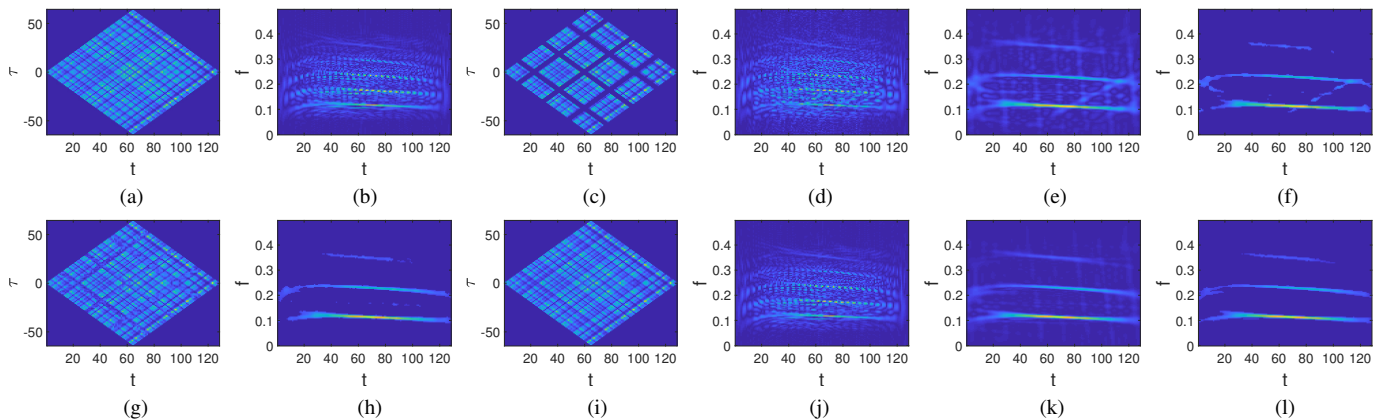


Fig. 9. Results for a real-life EEG seizure signal. (a) IAF in the absence of missing samples; (b) WVD in the absence of missing samples; (c) IAF with burst missing samples; (d) WVD with burst missing samples; (e) TFR using AOK with burst missing samples; (f) TFR using AOK and OMP with burst missing samples; (g) IAF recovered by atomic norm [30]; (h) TFR proposed in [30]; (i) IAF for stage 1 (patch-based ALOHA); (j) WVD for stage 1 (patch-based ALOHA) (k) TFR for stage 2 (patch based ALOHA + AOK); (l) The proposed AAO TFR (patch-based ALOHA + AOK + OMP).

better recovered as compared to Fig. 8(g). Correspondingly, the resulting WVD shown in Fig. 8(j) is close to the baseline WVD as well. After applying the AOK and OMP, a high-resolution TFR is obtained and is shown in Fig. 8(l). Again the superiority of the proposed AAO method is confirmed.

6) *Real-life EEG Seizure Signal*: IF estimation plays an important role in the phase synchrony measure for multi-channel EEG signals. In EEG signal processing, missing samples may occur due to the intentional removal of artifacts, such as the commonly observed eye blink, which usually takes between 100 and 500 ms. We consider a segment from newborn EEG seizure database, which consists of piecewise LFM signal components with harmonics [53], [54]. The total time period is 8 seconds which results in 128 samples. Three 375-ms (or 6-sample) data, separated by approximately 2 seconds, are removed as the result of eye blinks. The missing positions are 20 : 25, 57 : 62 and 94 : 99 samples, respectively.

The baseline IAF and WVD of the full-data signal are provided in Figs. 9(a) and 9(b). The corresponding results in the presence of burst missing samples are respectively presented in Figs. 9(c) and 9(d). It is observed that the cross-terms are difficult to be suppressed due to the strong artifacts induced by the burst missing samples, even after applying the

AOK and OMP, as depicted in Figs. 9(e) and 9(f).

The IAF obtained via the atomic-norm-based method fill in the missing entries to some extent, as indicated in Fig. 9(g). However, in Fig. 9(h), we notice that there are still some residual artifacts.

As shown in Fig. 9(i), the proposed ALOHA-based method recovers the missing IAF entries near perfectly. The corresponding WVD depicted in Fig. 9(j) is similar to the baseline WVD. In Figs. 9(k) and 9(l), we notice that with the further utilization of the AOK and OMP, the proposed method detects all three components with accurate IF estimates.

7) *Real-life Bat Echolocation Signal*: In the last example, we consider a real-life bat echolocation exponential chirp signal emitted by *Eptesicus fuscus*¹. The data contains 400 samples with a sampling period of $7 \mu\text{s}$. This pulse contains three harmonics, which are nearly linear in the logarithmic time [55]. We consider the same 40% of missing data as in the first five examples of Section V-A, rendering a total number of 160 missing samples.

¹The authors wish to thank C. Condon, K. White, and A. Feng of the Beckman Institute of the University of Illinois for the bat data and for permission to use it in this paper.

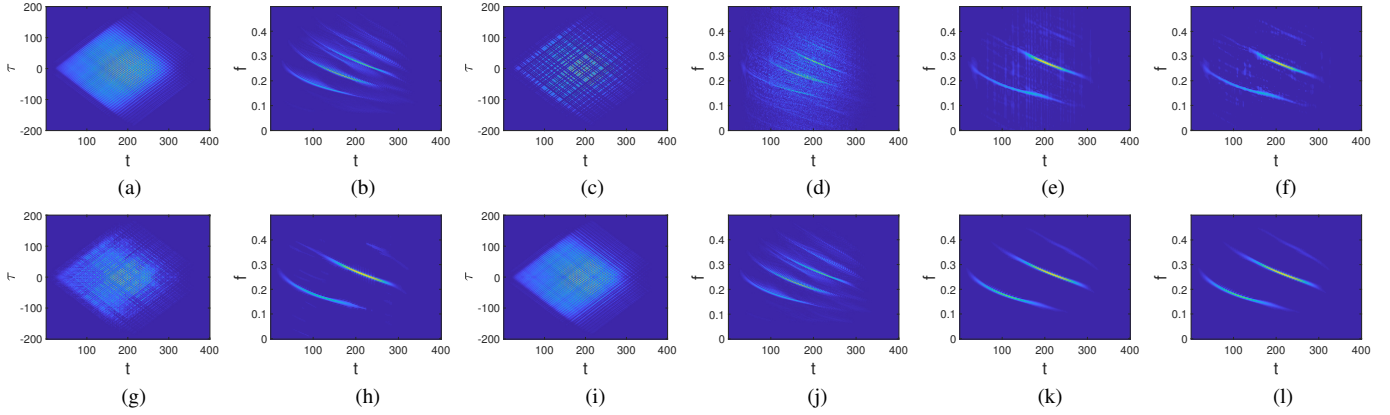


Fig. 10. Results for a real-life bat echolocation signal. (a) IAF in the absence of missing samples; (b) WVD in the absence of missing samples; (c) IAF with burst missing samples; (d) WVD with burst missing samples; (e) TFR using AOK with burst missing samples; (f) TFR using AOK and OMP with burst missing samples; (g) IAF recovered by atomic norm [30]; (h) TFR proposed in [30]; (i) IAF for stage 1 (patch-based ALOHA); (j) WVD for stage 1 (patch-based ALOHA); (k) TFR for stage 2 (patch based ALOHA + AOK); (l) The proposed AAO TFR (patch-based ALOHA + AOK + OMP).

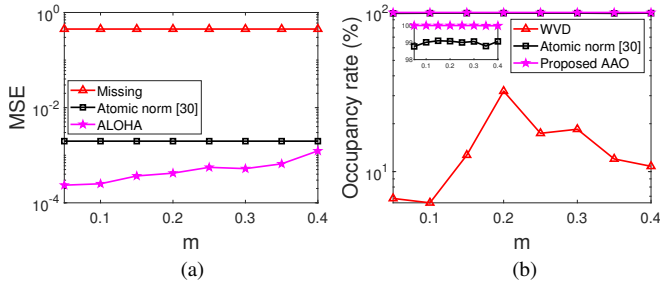


Fig. 11. Comparisons for two-component parallel LFM with various slopes m . (a) MSE of the IAF; (b) TFR occupancy rate (%).

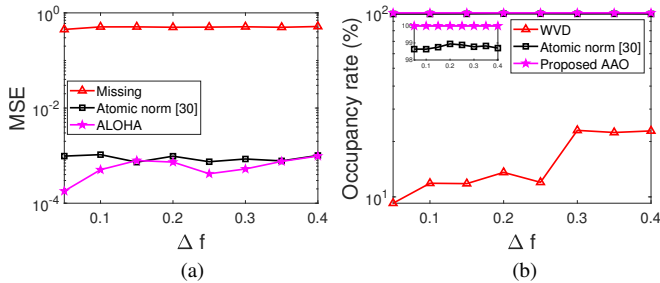


Fig. 12. Comparisons for two-component parallel LFM with various frequency differences Δf . (a) MSE of the IAF; (b) TFR occupancy rate (%).

The baseline IAF and WVD obtained from full-data pulse are provided in Fig. 10(a) and Fig. 10(b), respectively. The IAF and WVD obtained under burst missing samples are shown in Figs. 10(c) and 10(d), respectively. As observed in Figs. 10(e) and 10(f), artifacts still exist even after applying the AOK and OMP.

For the atomic norm-based method, we see that most of the missing IAF entries are filled properly and the resulting TFR consists of less artifacts, as depicted in Figs. 10(g) and 10(h). However, some residual artifacts exist due to the nonlinearity of the signal components. In Figs. 10(j) and 10(l), the results of the proposed method verify that all three harmonics are correctly recovered.

B. Energy Concentrations Analysis

In this subsection, we use the energy concentration measure to evaluate the seven case studies in Section V-A. The energy

TABLE III
COMPARISON OF ENERGY CONCENTRATIONS OF THE TFRS

	Case 1	Case 2	Case 3	Case 4	Case 5	Case 6	Case 7
WVD	61,407	75,850	70,336	75,531	71,091	59,591	717,331
[30]	1,811	1,847	1,636	1,930	2,617	1,164	3,773
AAO	1,581	1,796	1,579	1,807	2,306	1,143	3,491

concentration measure is defined as [56]:

$$EC = \left(\sum_{t=1}^T \sum_{f'=1}^{N_f} |\rho(t, f')|^{\frac{1}{q}} \right)^q, \quad q > 1, \quad (69)$$

where ρ is the normalized TFD such that

$$\sum_{t=1}^T \sum_{f'=1}^{N_f} |\rho(t, f')| = 1. \quad (70)$$

In addition, $f' = 1, \dots, N_f$ denotes the frequency bin index and N_f stands for the total number of frequency bins. A lower EC value represents higher energy concentration since a highly concentrated TFD occupies a smaller support region.

The energy concentration measures of the WVD, the atomic norm-based method [30], and the proposed AAO method are compared in Table III, where $q = 2$ is used. The proposed AAO method consistently provides the highest energy concentration for all examples being considered in Section V-A.

C. Robustness Analysis

In this subsection, we quantitatively compare the performance of the proposed AAO method with the WVD and the atomic norm-based method [30]. Because the implementation of IAF interpolation is vital to mitigate the artifacts due to burst missing samples, the mean squared error (MSE) between the interpolated IAF and the baseline IAF (obtained from the noiseless signal with no missing samples) is used as a performance indicator of IAF recovery. We also compare the occupancy rate of the auto-terms, where the TFR obtained from AOK using full data is used as the reference mask area of the auto-terms. Three factors, namely, frequency slope, frequency difference, and SNR, are discussed.

TABLE IV
MSE COMPARISON BETWEEN THE BASELINE IAF AND THE IAF OBTAINED WITH INCOMPLETE DATA (MISS), ATOMIC NORM-BASED IAF [30] (AT), AND THE PROPOSED ALOHA-BASED IAF

SNR (dB)	40.63%			50%		
	Miss	AT	ALOHA	Miss	AT	ALOHA
Inf	0.58	0.48	0.02	0.69	0.65	0.19
25	0.59	0.49	0.03	0.69	0.65	0.21
15	0.60	0.52	0.09	0.70	0.68	0.27
5	0.76	0.73	0.51	0.82	0.78	0.69

1) *Frequency Slope*: For a better focus on the frequency change, we choose a two-component parallel LFM signal with the following phase laws,

$$\begin{aligned}\phi_1(t) &= 2\pi \left(0.05t + \frac{m}{2}t^2/T \right), \\ \phi_2(t) &= 2\pi \left(0.10t + \frac{m}{2}t^2/T \right).\end{aligned}\quad (71)$$

Fig. 11(a) reports the MSE of the IAF with respect to the frequency slope. We notice that the slope does not affect the performance of IAF recovery via the atomic-norm based method in [30]. For the ALOHA-based method, the MSE slightly increases as the slope increases, but the MSE is still lower than the atomic norm counterpart [30].

The occupancy rate is compared in Fig. 11(b). We observe that the proposed method provides the highest TF occupancy rate compared with the WVD and the atomic norm-based TFR reconstruction method in [30].

2) *Frequency Difference*: Now we consider a two-component parallel LFM signal, where the frequency difference is a constant. The phase laws are expressed as

$$\begin{aligned}\phi_1(t) &= 2\pi (0.05t + 0.05t^2/T), \\ \phi_2(t) &= 2\pi (0.05t + \Delta f_0 t + 0.05t^2/T).\end{aligned}\quad (72)$$

Fig. 12(a) compares the MSE of the IAF with respect to the frequency difference. As discussed in Section IV-A, the ALOHA-based method consistently outperforms the atomic norm-based method in its IAF reconstruction performance. The improvement is more evident when the frequency difference Δf_0 is smaller.

3) *Signal-to-Noise Ratio*: We consider noisy signal measurements with different values of the input SNR and missing sample rate. 50 independent trials are performed for each scenario. For the convenience of presentation, we select the most challenging case with the instantaneous phase laws defined in (68), i.e., the signal consisting of one sinusoidal FM and one LFM. Two missing samples rates, i.e., 40.63% (52 missing samples) and 50% (64 missing samples), are considered.

As shown in Table IV, the proposed AAO method provides much lower MSE between the baseline IAF and the reconstructed IAF, especially in high SNR cases, compared to the method [30]. The occupancy rate of the auto-terms is compared in Table V. Compared to [30], the proposed method improves the TFR reconstruction performance with a higher occupancy rate.

TABLE V
TFR OCCUPANCY RATE (%) OF THE WVD, ATOMIC NORM-BASED TFR RECONSTRUCTION METHOD [30], AND THE PROPOSED AAO METHOD

SNR (dB)	40.63%			50%		
	WVD	[30]	AAO	WVD	[30]	AAO
Inf	38.39	85.82	99.25	13.17	70.87	90.14
25	32.02	78.37	95.20	11.37	70.52	88.99
15	31.79	76.73	94.53	10.69	69.73	86.38
5	30.73	70.68	89.08	10.37	61.79	75.54

VI. CONCLUSION

In this paper, we proposed a novel approach to achieve high-fidelity TFR reconstruction for multi-component FM signals with distinct amplitude differences in the presence of burst missing samples. We overcome the limitation of the existing sparsity-based TFR reconstruction methods that require cross-term presence to be sparse in the TF domain. We formulate the IAF reconstruction problem as a rank minimization problem of a block Hankel matrix that effectively mitigates the effects of burst missing samples and is robust to the amplitude differences between signal components. A data-adaptive TF kernel is then applied to further suppress the cross-terms and reduce the residual effects of missing samples. We provided performance analyses for different types of FM signals and a guiding rule for patch size optimization. Extensive simulation results were provided to verify the superiority of the proposed method over the existing state-of-the-art method.

REFERENCES

- [1] A. Papandreou-Suppappola Ed., *Applications in Time-Frequency Signal Processing*. Boca Raton, FL: CRC Press, 2002.
- [2] V. C. Chen and H. Ling, *Time-Frequency Transforms for Radar Imaging and Signal Analysis*. Norwood, MA: Artech House, 2002.
- [3] M. An, A. K. Brodzik, and R. Tolimieri, "Ideal sequence design in time-frequency space, applications to radar, sonar and communication systems," in *Applied and Numerical Harmonic Analysis*. Boston, MA: Birkhäuser, 2008.
- [4] L. Stankovic, M. Dakovic, and T. Thayaparan, *Time-Frequency Signal Analysis With Applications*. Boston, MA: Artech House, 2013.
- [5] Y. Chen, D. Joffre, and P. Avitabile, "Underwater dynamic response at limited points expanded to full-field strain response," *ASME J. Vib. Acoust.*, vol. 140, no. 5, pp. 051016-1–051016-9, Oct. 2018.
- [6] B. Boashash, "Estimating and interpreting the instantaneous frequency of a signal—Part 1: Fundamentals," *Proc. IEEE*, vol. 80, no. 4, pp. 520–538, Apr. 1992.
- [7] B. Boashash, "Estimating and interpreting the instantaneous frequency of a signal—Part 2: Algorithms and applications," *Proc. IEEE*, vol. 80, no. 4, pp. 540–568, Apr. 1992.
- [8] H. Zhang, G. Bi, W. Yang, S. G. Razul, and C. M. S. See, "IF estimation of FM signals based on time-frequency image," *IEEE Trans. Aerosp. Electron. Syst.*, vol. 51, no. 1, pp. 326–343, Jan. 2015.
- [9] B. Boashash and S. Ouelha, "An improved design of high-resolution quadratic time-frequency distributions for the analysis of nonstationary multicomponent signals using directional compact kernels," *IEEE Trans. Signal Process.*, vol. 65, no. 10, pp. 2701–2713, May 2017.
- [10] N. A. Khan, M. Mohammadi, and I. Stankovic, "Sparse reconstruction based on iterative TF domain filtering and Viterbi based IF estimation algorithm," *Signal Process.*, vol. 166, no. 107260, pp. 1–12, Jan. 2020.
- [11] B. Boashash (Ed.), *Time-Frequency Signal Analysis and Processing: A Comprehensive Reference, 2nd Ed.* San Diego, CA: Academic Press, 2015.
- [12] C. Liu, F. Xi, S. Chen, Y. D. Zhang, and Z. Liu, "Pulse-Doppler signal processing with quadrature compressive sampling," *IEEE Trans. Aerosp. Electron. Syst.*, vol. 51, no. 2, pp. 1217–1230, April 2015.

- [13] L. Stanković, "ISAR image analysis and recovery with unavailable or heavily corrupted data," *IEEE Trans. Aerosp. Electron. Syst.*, vol. 51, no. 3, pp. 2093–2106, July 2015.
- [14] B. Jokanovic and M. G. Amin, "Reduced interference sparse time-frequency distributions for compressed observations," *IEEE Trans. Signal Process.*, vol. 63, no. 24, pp. 6698–6709, Dec. 2015.
- [15] M. Turley, "Impulsive noise rejection in HF radar using a linear prediction technique," in *Proc. IEEE Int. Radar Conf.*, Adelaide, Australia, Sept. 2003.
- [16] C. J. Law, G. Jones, D. C. Backer, W. C. Barott, G. C. Bower, C. Gutierrez-Kraybill, P. K. G. Williams, and D. Werthimer, "Millisecond imaging of radio transients with the pocket correlator," *Astrophys. J.*, vol. 742, no. 12, pp. 1–13, Nov. 2011.
- [17] L. Stanković, T. Thayaparan, M. Daković, and V. Popović-Bugarin, "Micro-Doppler removal in radar imaging analysis," *IEEE Trans. Aerosp. Electron. Syst.*, vol. 49, no. 2, pp. 1234–1250, April 2013.
- [18] J. F. Gao, Y. Yang, P. Lin, P. Wang, and C. X. Zheng, "Automatic removal of eye-movement and blink artifacts from EEG signals," *Brain Topogr.*, vol. 2010, no. 23, pp. 105–114, 2010.
- [19] B. Singh and H. Wagatsuma, "A removal of eye movement and blink artifacts from EEG data using morphological component analysis," *Comput. Math. Methods Medicine*, vol. 2017, no. 1861645, pp. 1–17.
- [20] Y. D. Zhang, M. G. Amin, and B. Himed, "Reduced interference time-frequency representations and sparse reconstruction of undersampled data," in *Proc. European Signal Process. Conf.*, Marrakech, Morocco, Sept. 2013, pp. 1–5.
- [21] I. Orovic, S. Stankovic, and T. Thayaparan, "Time frequency-based instantaneous frequency estimation of sparse signals from incomplete set of samples," *IET Signal Process.*, vol. 8, no. 3, pp. 239–245, May 2014.
- [22] M. G. Amin, B. Jakonovic, Y. D. Zhang, and F. Ahmad, "A sparsity-perspective to quadratic time-frequency distributions," *Digit. Signal Process.*, vol. 46, pp. 175–190, Nov. 2015.
- [23] S. Liu, Y. D. Zhang, T. Shan, and R. Tao, "Structure-aware Bayesian compressive sensing for frequency-hopping spectrum estimation with missing observations," *IEEE Trans. Signal Process.*, vol. 66, no. 8, pp. 2153–2166, April 2018.
- [24] B. Jokanovic, M. Amin, and T. Dogaru, "Time-frequency signal representations using interpolations in joint-variable domains," *IEEE Trans. Geosci. Remote Sens.*, vol. 12, no. 1, pp. 204–208, Jan. 2015.
- [25] Y. D. Zhang, "Resilient quadratic time-frequency distribution for FM signals with gapped missing data," in *Proc. IEEE Radar Conf.*, Seattle, WA, May 2017, pp. 1765–1769.
- [26] V. S. Amin, Y. D. Zhang, and B. Himed, "Sparsity-based time-frequency representation of FM signals with burst missing samples," *Signal Process.*, vol. 155, pp. 25–43, Feb. 2019.
- [27] V. S. Amin, Y. D. Zhang, and B. Himed, "Improved instantaneous frequency estimation of multi-component FM signals," in *Proc. IEEE Radar Conf.*, Boston, MA, Apr. 2019.
- [28] P. Stoica, J. Li, and J. Ling, "Missing data recovery via a non-parametric iterative adaptive approach," *IEEE Signal Process. Lett.*, vol. 16, no. 4, pp. 241–244, Apr. 2009.
- [29] Y. Chi, L. L. Scharf, A. Pezeshki, and A. R. Calderbank, "Sensitivity to basis mismatch in compressed sensing," *IEEE Trans. Signal Process.*, vol. 59, no. 5, pp. 2182–2195, May 2011.
- [30] S. Zhang and Y. D. Zhang, "Robust time-frequency analysis of multiple FM signals with burst missing samples," *IEEE Signal Process. Lett.*, vol. 26, no. 8, pp. 1172–1176, June 2019.
- [31] D. L. Jones and R. G. Baraniuk, "An adaptive optimal kernel time-frequency representation," *IEEE Trans. Signal Process.*, vol. 43, no. 10, pp. 2361–2371, Oct. 1995.
- [32] J. A. Tropp and A. C. Gilbert, "Signal recovery from random measurements via orthogonal matching pursuit," *IEEE Trans. Inf. Theory*, vol. 53, no. 12, pp. 4655–4666, Dec. 2007.
- [33] K. H. Jin and J. C. Ye, "Annihilating filter based low rank Hankel matrix approach for image inpainting," *IEEE Trans. Image Process.*, vol. 24, no. 11, pp. 3498–3511, Nov. 2015.
- [34] J. Min, L. Carlini, M. Unser, S. Manley, and J. C. Ye, "Fast live cell imaging at nanometer scale using annihilating filter based low rank Hankel matrix approach," *Proc. SPIE*, San Diego, CA, vol. 9597, no. 95970V, Sept. 2015.
- [35] K. H. Jin, D. Lee, and J. C. Ye, "A general framework for compressed sensing and parallel MRI using annihilating filter based low-rank Hankel matrix," *IEEE Trans. Comput. Imag.*, vol. 2, no. 4, pp. 480–495, Dec. 2016.
- [36] S. Razavikia, A. Amini and S. Daei, "Reconstruction of binary shapes from blurred images via Hankel-structured low-rank matrix recovery," *IEEE Trans. Image Process.*, vol. 29, pp. 2452–2462, Nov. 2019.
- [37] K. H. Jin and J. C. Ye, "Sparse and low-rank decomposition of a Hankel structured matrix for impulse noise removal," *IEEE Trans. Image Process.*, vol. 27, no. 3, pp. 1448–1461, Mar. 2018.
- [38] N. A. Khan and B. Boashash, "Multi-component instantaneous frequency estimation using locally adaptive directional time frequency distributions," *Int. J. Adaptive Control Signal Process.*, vol. 30, pp. 429–442, Mar. 2016.
- [39] N. A. Khan and M. Mohammadi, "Reconstruction of nonstationary signals with missing samples using time-frequency filtering," *Circuits Syst. Signal Process.*, vol. 37, no. 8, pp. 3175–3190, 2018.
- [40] H. I. Choi and W. J. Williams, "Improved time-frequency representation of multicomponent signals using exponential kernels," *IEEE Trans. Acoust. Speech Signal Process.*, vol. 37, no. 6, pp. 862–871, June 1989.
- [41] Y. Zhao, L. E. Atlas, and R. J. Marks, "The use of cone-shaped kernels for generalized time-frequency representations of nonstationary signals," *IEEE Trans. Acoust. Speech Signal Process.*, vol. 38, no. 7, pp. 1084–1091, July 1990.
- [42] V. Chandrasekaran, B. Recht, P. A. Parrilo, and A. S. Willsky, "The convex geometry of linear inverse problems," *Found. Comput. Math.*, vol. 12, no. 6, pp. 805–849, Dec. 2012.
- [43] Y. Li and Y. Chi, "Off-the-grid line spectrum denoising and estimation with multiple measurement vectors," *IEEE Trans. Signal Process.*, vol. 64, no. 5, pp. 1257–1269, Mar. 2016.
- [44] M. Vetterli, P. Marziliano, and T. Blu, "Sampling signals with finite rate of innovation," *IEEE Trans. Signal Process.*, vol. 50, no. 6, pp. 1417–1428, June 2002.
- [45] J. C. Ye, J. M. Kim, K. H. Jin and K. Lee, "Compressive sampling using annihilating filter-based low-rank interpolation," *IEEE Trans. Inf. Theory*, vol. 63, no. 2, pp. 777–801, Feb. 2017.
- [46] J. Min, K. H. Jin, M. Unser, and J. C. Ye, "Grid-free localization algorithm using low-rank hankel matrix for super-resolution microscopy," *IEEE Trans. Image Process.*, vol. 27, no. 10, pp. 4771–4786, June 2018.
- [47] Y. Chen and Y. Chi, "Harnessing structures in big data via guaranteed low-rank matrix estimation: recent theory and fast algorithms via convex and nonconvex optimization," *IEEE Signal Process. Mag.*, vol. 35, no. 4, pp. 14–31, July 2018.
- [48] E. Candes and Y. Plan, "Matrix completion with noise," *Proc. IEEE*, vol. 98 no. 6 pp. 925–936, June 2010.
- [49] S. Boyd, N. Parikh, E. Chu, B. Peleato, and J. Eckstein, "Distributed optimization and statistical learning via the alternating direction method of multipliers," *Found. Trends Mach. Learn.*, vol. 3, no. 1, pp. 1–122, Jan. 2011.
- [50] M. Signoretto, V. Cevher, and J. A. K. Suykens, "An SVD-free approach to a class of structured low rank matrix optimization problems with application to system identification," in *Proc. IEEE Conf. Decision Control*, Dec. 2013, pp. 1–6.
- [51] P. Flandrin and P. Borgnat, "Time-frequency energy distributions meet compressed sensing," *IEEE Trans. Signal Process.*, vol. 58, no. 6, pp. 2974–2982, June 2010.
- [52] R. J. Tibshirani, "Regression shrinkage and selection via the LASSO," *J. Royal Statistical Soc.*, vol. 58, no. 1, pp. 267–288, 1996.
- [53] B. Boashash, N. A. Khan, and T. Ben-Jabeur, "Time-frequency features for pattern recognition using high-resolution TFDs: A tutorial review," *Digit. Signal Process.*, vol. 40, pp. 1–30, 2015.
- [54] N. Khan and S. Ali, "A robust and efficient instantaneous frequency estimator of multi-component signals with intersecting time-frequency signatures," *Signal Process.*, vol. 177, 2020.
- [55] A. R. Wheeler, K. A. Fulton, J. E. Gaudette, R. A. Simmons, I. Matsuo, and J. A. Simmons, "Echolocating big brown bats, *Eptesicus fuscus*, modulate pulse intervals to overcome range ambiguity in cluttered surroundings," *Frontiers Behav. Neurosci.*, vol. 10, no. 125, June 2016.
- [56] L. Stanković, "A measure of some time-frequency distributions concentration," *Signal Process.*, vol. 81, no. 3, pp. 621–631, Mar. 2001.